Astronomy & Astrophysics manuscript no. PaperCND
November 16, 2010
© ESO 2010

arXiv:1011.3271v1 [astro-ph.GA] 15 Nov 2010

Mapping photodissociation and shocks in the vicinity of Sgr A*

M. A. Amo-Baladrón[1], J. Martín-Pintado[1], and S. Martín[2,3]

[1] Centro de Astrobiología (CSIC/INTA), Ctra. de Torrejón a Ajalvir km 4, E-28850, Torrejón de Ardoz, Madrid, Spain
e-mail: arancha@damir.iem.csic.es
[2] European Southern Observatory, Alonso de Córdova 3107, Vitacura, Casilla 19001, Santiago 19, Chile
[3] Harvard-Smithsonian Center for Astrophysics, 60 Garden Street, Cambridge, MA 02138, USA

Received —; accepted —

ABSTRACT

Aims. We study the chemistry in the harsh environments of galactic nuclei using the nearest one, the Galactic center (GC).
Methods. We have obtained maps of the molecular emission within the central five arcminutes (12 pc) of the GC in selected molecular tracers: SiO(2–1), HNCO($5_{0,5}$–$4_{0,4}$), and the $J = 1 \rightarrow 0$ transition of $H^{13}CO^+$, $HN^{13}C$, and $C^{18}O$ at an angular resolution of 30″ (1.2 pc). The mapped region includes the circumnuclear disk (CND) and the two surrounding giant molecular clouds (GMCs) of the Sgr A complex, known as the 20 and 50 km s^{-1} molecular clouds. Additionally, we simultaneously observed the $J = 2 \rightarrow 1$ and $J = 3 \rightarrow 2$ transitions of SiO toward selected positions to estimate the physical conditions of the molecular gas using the large velocity gradient approximation.
Results. The SiO(2–1) emission shows all the molecular features identified in previous studies, covering the same velocity range as the $H^{13}CO^+$(1–0) emission, which also presents a similar distribution. In contrast, HNCO(5–4) emission appears in a narrow velocity range mostly concentrated in the 20 and 50 km s^{-1} GMCs. A similar trend follows the $HN^{13}C$(1–0) emission. The HNCO column densities and fractional abundances present the highest contrast, with difference factors of ≥60 and 28, respectively. Their highest values are found toward the cores of the GMCs, whereas the lowest ones are measured at the CND. SiO abundances do not follow this trend, with high values found toward the CND, as well as the GMCs. By comparing our abundances with those of prototypical Galactic sources we conclude that HNCO, similar to SiO, is ejected from grain mantles into gas-phase by nondissociative C-shocks. This results in the high abundances measured toward the CND and the GMCs. However, the strong UV radiation from the Central cluster utterly photodissociates HNCO as we get closer to the center, whereas SiO seems to be more resistant against UV-photons or it is produced more efficiently by the strong shocks in the CND. This UV field could be also responsible for the trend found in the $HN^{13}C$ abundance.
Conclusions. We discuss the possible connections between the molecular gas at the CND and the GMCs using the HNCO/SiO, SiO/CS, and HNCO/CS intensity ratios as probes of distance to the Central cluster. In particular, the HNCO/SiO intensity ratio is proved to be an excellent tool for evaluating the distance to the center of the different gas components.

Key words. astrochemistry – Galaxy: abundances – Galaxy: center – Galaxy: nucleus – ISM: clouds – ISM: molecules

1. Introduction

Its proximity (8.0±0.5 kpc; Reid 1993) makes the Galactic center (GC) the best laboratory for understanding the heating and chemistry of the interstellar medium (ISM) in the harsh environment of galaxy nuclei. Just in its central 5 arcmin (12 pc), one can find a massive black hole surrounded by a rotating circumnuclear disk (CND) of dust and gas, H II regions, massive stellar clusters, two supernova remants (SNRs), and two giant molecular clouds (GMCs). All these features coexist, interact, and can be spatially resolved at a resolution currently impossible even in the nearest extragalactic nucleus.

At its dynamical center, the GC harbors a massive black hole of $\sim 4.0 \times 10^6$ $M_\odot$ (Ghez et al. 2005) that is associated with the strong compact source of nonthermal emission Sgr A*, visible in radio continuum maps (Yusef-Zadeh & Morris 1987). Converging to Sgr A*, there are arc-shaped ionized gas streamers with a minispiral morphology (Sgr A West) that seem to be feeding the nucleus (Lo & Claussen 1983; Roberts & Goss 1993). Both the black hole and Sgr A West are surrounded by a ring of molecular gas and dust (the CND; Becklin et al. 1982; Güsten et al. 1987), whose inner edge suffers UV-photoionization (Roberts & Goss 1993) due to a dense stellar population of massive stars in the Central cluster (Krabbe et al. 1995; Figer 2008).

The CND has been observed from radio to infrared wavelengths in molecular gas tracers, continuum, and atomic species (see Table 1 for references). These studies have characterized the CND as dense ($\sim 10^{5-6}$ cm^{-3}; Marr et al. 1993; Marshall et al. 1995), clumpy, and very turbulent (with large linewidths). It extends from its inner edge, 1.6 pc from Sgr A*, to ≳2 pc, according to interferometric studies (Wright et al. 2001; Christopher et al. 2005), and it has an inclination (rotation axis from the line of sight; LOS) of about 60°–70°, with the major axis aligned approximately along the Galactic plane (position angle of ∼30° east of north; Güsten et al. 1987; Jackson et al. 1993; Marshall et al. 1995). The gas is mov-

⋆ Figures 3–7 and 13 are only available in the online version via http://www.edpsciencies.org

⋆⋆ Based on observations with the IRAM 30-m telescope. IRAM is supported by CNRS/INSU (France), the MPG (Germany) and the IGN (Spain).

Table 1. Observations of the CND

Tracers	References
H_2	Gatley et al. (1986)
	Yusef-Zadeh et al. (2001)
CO(1–0)	Liszt et al. (1985)
	Serabyn et al. (1986)
	Liszt & Burton (1995)
^{13}CO and C^{18}O(2–1)	Zylka et al. (1990)
CO(3–2)	Sutton et al. (1990)
	Dent et al. (1993)
	Liszt & Burton (1995)
CO(7–6)	Bradford et al. (2005)
CS(2–1)	Serabyn et al. (1986)
C^{34}S(2–1)	Zylka et al. (1990)
CS(7–6)	Montero-Castaño et al. (2009)
HCN(1–0)	Güsten et al. (1987)
	Marr et al. (1993)
	Wright et al. (2001)
	Christopher et al. (2005)
HCN(3–2)	Jackson et al. (1993)
	Marshall et al. (1995)
HCN(4–3)	Marshall et al. (1995)
	Montero-Castaño et al. (2009)
H^{13}CN(1–0)	Marr et al. (1993)
HCO$^+$(1–0)	Marr et al. (1993)
	Wright et al. (2001)
	Christopher et al. (2005)
	Shukla et al. (2004)
NH_3(1,1) (2,2)	Coil & Ho (1999, 2000)
NH_3(1,1) (2,2) (3,3)	McGary et al. (2001)
NH_3(6,6)	Herrnstein & Ho (2002)
Continuum at	Mezger et al. (1989)
mm and sub-mm	Zylka et al. (1990)
wavelengths	Davidson et al. (1992)
	Dent et al. (1993)
	Telesco et al. (1996)
Atomic species	Liszt et al. (1985)
(H I,[O I],[C I],[C II])	Genzel et al. (1985)
	Lugten et al. (1986)
	Jackson et al. (1993)
	Serabyn et al. (1994)

ing in circular orbits, rotating around the nucleus with a velocity of 110 km s^{-1} (Liszt et al. 1985; Marr et al. 1993), but it also presents noncircular motions (e.g.: Güsten et al. 1987; Jackson et al. 1993; Marshall et al. 1995; Shukla et al. 2004; Christopher et al. 2005). The CND does not appear to be an equilibrium structure. It seems to consist of several separated streamers in rotation around the nucleus (Jackson et al. 1993; Wright et al. 2001). Virial analysis suggests that the CND could be composed of high-density clumps ($\sim 10^{6-7}$ cm^{-3}) that could withstand the tidal shear making the CND a long-lived structure (Jackson et al. 1993; Shukla et al. 2004; Christopher et al. 2005; Montero-Castaño et al. 2009). However, Güsten et al. (1987) derived significantly lower densities ($\sim 10^5$ cm^{-3}) from their interferometric mapping of HCN, which are consistent with the densities estimated from warm atomic gas (Genzel et al. 1985) and CO multitransitional observations (Harris et al. 1985).

One question that remains without a conclusive answer is how the CND is fed. Since this structure is not just a transient feature losing material through infall (probably via Sgr A West, Montero-Castaño et al. 2009), there must be gas feeding the disk. Two GMCs that lie near the GC are the best candidates to feed the CND: the 20 km s^{-1} and the 50 km s^{-1} GMCs (M−0.13−0.08 and M−0.02−0.07, respectively; Güsten et al. 1981; Güsten & Henkel 1983). Both are connected by a ridge of compressed dust and gas that warps around the SNR Sgr A East. This SNR lies behind or contains Sgr A West and appears as an expanding shell of synchrotron emission in radio continuum maps (Yusef-Zadeh & Morris 1987; Pedlar et al. 1989). But it is not the only SNR in the region. G 359.92−0.09, located to the south of Sgr A East (centered at $\Delta\alpha = 120''$, $\Delta\delta = -180''$ with respect to Sgr A*), is expanding into Sgr A East producing its concave southeastern edge (Coil & Ho 2000). Both SNRs seem to interact with the surrounding material pushing it away from or toward the nucleus. As a result, several streamers of gas and dust that could be feeding the CND have been formed (Lee et al. 2008).

Several studies at different wavelengths have attempted to establish the relation between all the components in the Sgr A complex and their 3-dimensional (3D) location (see Coil & Ho 2000; Herrnstein & Ho 2005; Lee et al. 2008, and references therein). For the sake of clarity, we show in Fig. 1 a 2D sketch of the region with all the previous identified components, following the notation of Herrnstein & Ho (2005) for the molecular features in most of the cases. These studies have resulted in the following picture:

1. The H II region Sgr A West, also known as the Minispiral, is located in front of or inside the SNR Sgr A East (Yusef-Zadeh & Morris 1987; Pedlar et al. 1989). Moreover, Maeda et al. (2002) place Sgr A*, Sgr A West, and the CND (hereafter the nuclear region) just inside the leading edge of Sgr A East.
2. The SNR Sgr A East is pushing the 50 km s^{-1} GMC both to the east and behind the SNR along the LOS (Coil & Ho 2000; Park et al. 2004).
3. The 20 km s^{-1} GMC is located in front of the nucleus along the LOS (Güsten & Downes 1980; Park et al. 2004) and Sgr A East could also be expanding into this GMC (Mezger et al. 1989).
4. Both GMCs are connected by the Molecular Ridge, whose northern part is farther away from the Sun along the LOS than the southern part (Coil & Ho 2000). Lee et al. (2008) claim that the SNR Sgr A East could interact with the northern part of the ridge nearly perpendicular to the LOS, locating the northern part of the ridge slightly behind this SNR.
5. The SNR G 359.92−0.09 is interacting with the southern part of the Molecular Ridge, the eastern edge of the 20 km s^{-1} GMC, and the southern edge of Sgr A East (Coil & Ho 2000).
6. The Western Streamer, a ridge of emission seen in NH_3 bordering the western edge of Sgr A East, is highly inclined with respect to the LOS, and it is expanding outward as does this SNR (McGary et al. 2001; Lee et al. 2008).
7. The CND could be connected with the GMCs through three molecular gas streamers: the Southern Streamer (Okumura et al. 1991), the Northern Ridge (McGary et al. 2001), and the 50 km s^{-1} Streamer (Szczepanski et al. 1991).
8. Finally, high-velocity C^{18}O(2−1) emission between −80 and 20 km s^{-1} located in projection close to the nuclear region have been identified by Genzel et al. (1990). In our maps,

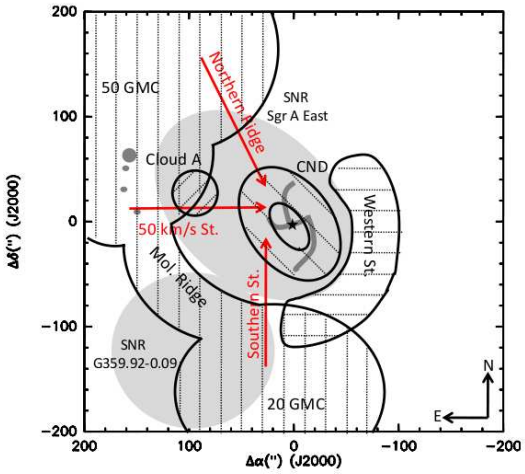

Fig. 1. Sketch of the 12 central parsecs of the Galaxy. Gray regions represents radio continuum features. Big ellipses correspond to the SNRs Sgr A East and G 359.92−0.09, the central minispiral to the H II region Sgr A West, and the four little circles to the Sgr A East compact H II regions. The central star represents Sgr A*. Molecular gas features are represented by stripped regions, whereas red arrows toward the center point out the possible connections between the CND (the elliptic disk) and the CMCs of this region. See the text for more details.

this emission appears as a small blue-shifted molecular cloud that we will refer it to as Cloud A.

The main heating mechanism in this complex region (CND and its central cavity) seems to be a combination of photoelectric heating by UV photons and mechanical heating by dissipation of supersonic turbulence in shocks (Bradford et al. 2005; Montero-Castaño et al. 2009). Theoretical models for the formation of the CND and the Northern Arm of the ionized Minispiral invoke infalling clouds as a result of cloud-cloud collisions and predict frequent collisions between clumps that would produce shock heating (Sanders 1998; Vollmer & Duschl 2002). Direct probes of shocks in the CND are the detections of 1720 MHz OH masers with extreme velocities (±130 km s^{-1}) at its lobes reported by Sjouwerman & Pihlström (2008). These authors claim that this type of maser is collisionally pumped and originates in postshock regions. Bradford et al. (2005), modeling CO rotational lines, reached the conclusion that UV heating alone is not able to match the CO luminosities, and therefore mechanical energy dissipated into the gas in low-velocity (10–20 km s^{-1}) C-shocks with magnetic fields of 0.3–0.5 mG could be the primary source of energy for the bulk of the heating of the CND material. Additional probes of shocks and/or UV radiation come from prominent H_2 emission found in the CND, in its southwest and northeast lobes, just where HCN(1–0) emission is stronger (Christopher et al. 2005). Moreover, there could be another source of shocks in the CND. In their study of the possible interactions between Sgr A East and the molecular gas features of the nuclear region, Lee et al. (2008) have found that the southern part of the CND and its northwestern region could lie in front of the SNR Sgr A East and could be pushed toward us. In fact, several 1720 MHz OH masers have been detected tracing the interaction of this SNR with the surrounding GMCs (Sjouwerman & Pihlström 2008).

Therefore, the energetics of the central region seem to be dominated by UV radiation and magnetohydrodynamical shocks. Chemical complexity can potentially be used to locate the different molecular components along the LOS in the central region by measuring the effects of photodissociation produced by the UV radiation from the Central cluster. It has been proposed that SiO, HNCO, and CS are among the best molecular tracers of the different ISM heating mechanisms. All of them have high critical densities suitable for GC physical conditions, so they trace similar gas components, but each species is sensitive to different heating mechanisms through their particular chemistry. SiO is a well-known shock tracer (Martín-Pintado et al. 1992), HNCO seems to be also associated to grain chemistry but it is strongly affected by photodissociation (Martín et al. 2008, 2009a), whereas CS is marginally enhanced in UV (Goicoechea et al. 2006; Martín et al. 2008) and shocked environments (Requena-Torres et al. 2006). The SiO/CS and HNCO/CS ratios can then be used to trace shocks in well-shielded regions by the enhancement of the SiO and HNCO abundances with respect to that of CS. In unshielded regions illuminated by UV radiation and with strong shocks, one expects to measure an enhancement of the SiO/CS ratio and the decrease in the HNCO/CS ratio.

In this paper we present spectral imaging of the molecular emission from the central region of the GC (12 pc), which includes the CND and two GMCs of the Sgr A complex. The selected molecular lines were the $J = 2 \rightarrow 1$ transition of SiO, the $J = 5_{0,5} \rightarrow 4_{0,4}$ transition of HNCO (hereafter HNCO(5–4)), and the $J = 1 \rightarrow 0$ transition of $H^{13}CO^+$, $HN^{13}C$, and ^{18}CO. In Sect. 2 the observation and data reduction procedures are described. Sect. 3 presents the data for each observed species in selected velocity ranges for better comparison with radio continuum maps. Kinematics is described with declination-velocity maps at constant right ascension intervals. Physical conditions at selected positions, as well as column densities and fractional abundances, are derived in Sects. 4 and 5. Finally, in Sect. 6 the changes found in molecular abundances are discussed, compared to prototypical sources, and used to probe the different heating mechanisms in the region and to establish the location of the different molecular components in the nuclear region relative to the Central cluster.

2. Observations

The observations were carried out with the IRAM-30m radiotelescope at Pico Veleta (Spain) during the summer of 2006. The mapping of the lines were made simultaneously by tuning the two 3 mm receivers (A and B) to two different frequencies: 86.892 and 109.905 GHz. Within the first frequency band we observed the SiO(2–1), $H^{13}CO^+$(1–0), and $HN^{13}C$(1–0) lines, whereas within the second frequency band we observed the HNCO(5–4) and $C^{18}O$(1–0) lines. Both receivers were tuned to a single sideband with image rejections of 30 dB and 25 dB. The system temperatures ranged between 154–176 K and 222–265 K during the observations for the lower and higher frequency setups, respectively. We used filterbanks (512 × 1 MHz) as spectrometers, providing a spectral resolution of 3.4 km s^{-1} at 86.9 GHz, and 2.7 km s^{-1} at 109.9 GHz, enough to resolve the wide emission lines of the GC (∼20 km s^{-1}).

Data were taken using the on-the-fly (OTF) technique with a telescope dump time (integration time on each position) of 1 s and was fully sampled at 86.9 GHz. The maps cover an area of 300″ × 300″ (12 × 12 pc at the GC distance of

8.0 kpc) centered on the position of the radio source Sgr A* ($(\alpha, \delta)_{J2000}$= $17^d45^m40^s.031$, $-29°00'28''.58$). We made eight coverages of the region alternating the scanning direction between right ascension and declination. The orthogonal covers were made in such a way that the $\sim 200'' \times 200''$ central region was finally mapped in both directions, in order to minimize possible scanning artifacts. The half-power beamwidth (HPBW) of the telescope was 28″ at the frequency of 86.9 GHz, and 22″ at 109.9 GHz.

Spectra were calibrated using the standard dual load system. We used the antenna temperature scale (T_A^*) for the line intensities because the emission is rather extended and fills the beam. We used (l, b)=$(-0.02°, -0.20°)$ as reference position, close enough to minimize the time lost due to telescope switching and differences in atmospheric airmass. This position shows almost no emission in the CS(1–0) survey of Tsuboi et al. (1999). To confirm that the reference was free of emission, it was checked against another further reference ((l, b)=$(-0.25°, -0.25°)$). The reference position shows no emission at a noise level of 12 and 23 mK for the low and high frequency spectra, respectively. A focus check was performed at the beginning of each observing session, and pointing was checked at the beginning and in the middle of each observing session.

Data reduction was done with the GILDAS package. The reduction process was as follows. First, bad channels and standing waves were removed from the spectra, and typical baselines up to order 3, in the case of spectra at 86.9 GHz, and up to order 5, at 109.9 GHz, were subtracted. In the case of the high-frequency spectra, a baseline of order 0 would had been enough, but a baseline of higher degree was needed to correct the baseline at the backend edges. We also used the CS data cube of the $J = 1 \rightarrow 0$ line taken by Tsuboi et al. (1999). To make all our molecular line cubes and that of CS(1–0) comparable, our spectra were resampled to the same velocity resolution as for the CS(1–0) cube (5 km s^{-1}). Finally, we constructed all the molecular line maps with an HPBW of 30″ (the beam of the 86.9 GHz and CS(1–0) cubes). The final data cubes have an rms noise per channel of 27, 37, and 100 mK for the SiO/$H^{13}CO^+$/$HN^{13}C$, HNCO/$C^{18}O$, and CS lines, respectively.

We also present observations of the $J = 2 \rightarrow 1$ and $J = 3 \rightarrow 2$ transitions of SiO taken simultaneously at selected positions. The HPBW of the telescope at the rest frequency of the SiO(3–2) transition (130.26861 GHz) was 19″. The system temperature was around 150 for the (2–1) and 270 K for (3–2) transitions, resulting in an rms noise $\leq$32 mK. The (40″, −120″) position was observed in a past campaign and presents system temperatures of 278 and 423 K, and rms noise values of 56 and 80 mK for the (2–1) and (3–2) transitions.

3. Results

In this section we analyze the morphology and kinematics of the emission for every observed molecular species. Figure 2 shows the integrated intensity maps of the observed molecular lines in 9 velocity intervals, from −125 to 130 km s^{-1}, selected to highlight the different components seen in the data cubes (velocity-channel maps are available in the online version Figs. A.1–A.5). In this figure, we also show the CS(1–0) integrated intensity maps of Tsuboi et al. (1999) for comparison. The rms noise for the integrated-velocity maps ($\sigma_{\Delta v}$) has been calculated from the rms noise of the original data cubes (σ_{ch}; Sect. 2) using the formula

$$\sigma_{\Delta v} = \frac{\sigma_{ch}}{\sqrt{N_{ch}}} \cdot \Delta v \quad (1)$$

where N_{ch} is the number of integrated velocity channels and Δv the velocity range where the emission is integrated.

Figure 3 shows declination-velocity maps at constant right ascension. To increase the signal-to-noise ratio and to clearly show the gas kinematics of the components associated with the most outstanding features, we have also averaged the declination-velocity cuts at four selected right ascension intervals.

Finally, in Fig. 4 we compare the integrated SiO(2–1) emission maps with the radio continuum image at 6 cm (Yusef-Zadeh & Morris 1987), where we can distinguish the thermal emission from Sgr A West (the gray minispiral in Fig. 1). This feature is composed of three ionized gas streamers: the Western Arc (the southwestern photoionized inner edge of the CND; Serabyn & Lacy 1985), and the Northern and Eastern Arms (infalling ionized gas that has been stripped off of the CND or has originated outside the CND; Lo & Claussen 1983; Roberts & Goss 1993).

3.1. The SiO(2–1) data cube.

The SiO(2–1) emission appears above the 3σ level in a wide velocity range: from −125 km s^{-1}, where the emission shows up in the southwest (relative to the position of Sgr A*) to 130 km s^{-1}, where the emission disappears in the northeast. The SiO(2–1) morphology shows the kinematics of the rotating CND. The southern and northern lobes are located at the ends of the major axis with the maximum LOS velocities, and the gas with the lower radial velocities is located in the minor axis (Marshall et al. 1995). The velocity pattern of the CND can be clearly seen in Fig. 3 at the RA= [−45″, 45″] cut. The derived velocity gradient is $\sim$2.2 km s^{-1} arcsec^{-1} ($\sim$60 km s^{-1} pc^{-1}). The southern lobe is stronger than the northern one, as in the case of all the previously HCN observations. SiO also shows the extension to the southwest detected by Marshall et al. (1995) in HCN(3–2), which is very likely the southernmost part of the Western Streamer, as discussed later. The inclination of the CND traced by the SiO emission agrees with previous observations, with the major axis aligned along the Galactic plane.

Figure 5 shows a composition of the velocity-integrated maps of the SiO(2–1) emission at the extreme CND velocities, [−50, −20] km s^{-1} and [70, 100] km s^{-1}, and the HCN(4–3) interferometric map of the CND obtained by Montero-Castaño et al. (2009) smoothed to 15″ resolution. This clearly shows that the SiO(2–1) emission completely traces the CND.

In the most extreme blueshifted velocity ranges ([−125, −50] km s^{-1}), the SiO(2–1) line presents maximum emission at three locations: (−15″, −30″), (95″, 25″), and (−40″, −70″). The first peak emission correspond to the southwest lobe of the CND (labeled as SW CND in Fig. 4; see also Fig. 5). The maximum at (95″, 25″) belongs to Cloud A (see Sect. 6.7), a small molecular cloud that seems to be isolated from the surrounding molecular gas (see also the declination-velocity plot at RA= [45″, 105″] in Fig. 3). In the [−95, −50] km s^{-1} panel of Fig. 4 we can appreciate that this cloud is located inside the eastern edge of the SNR

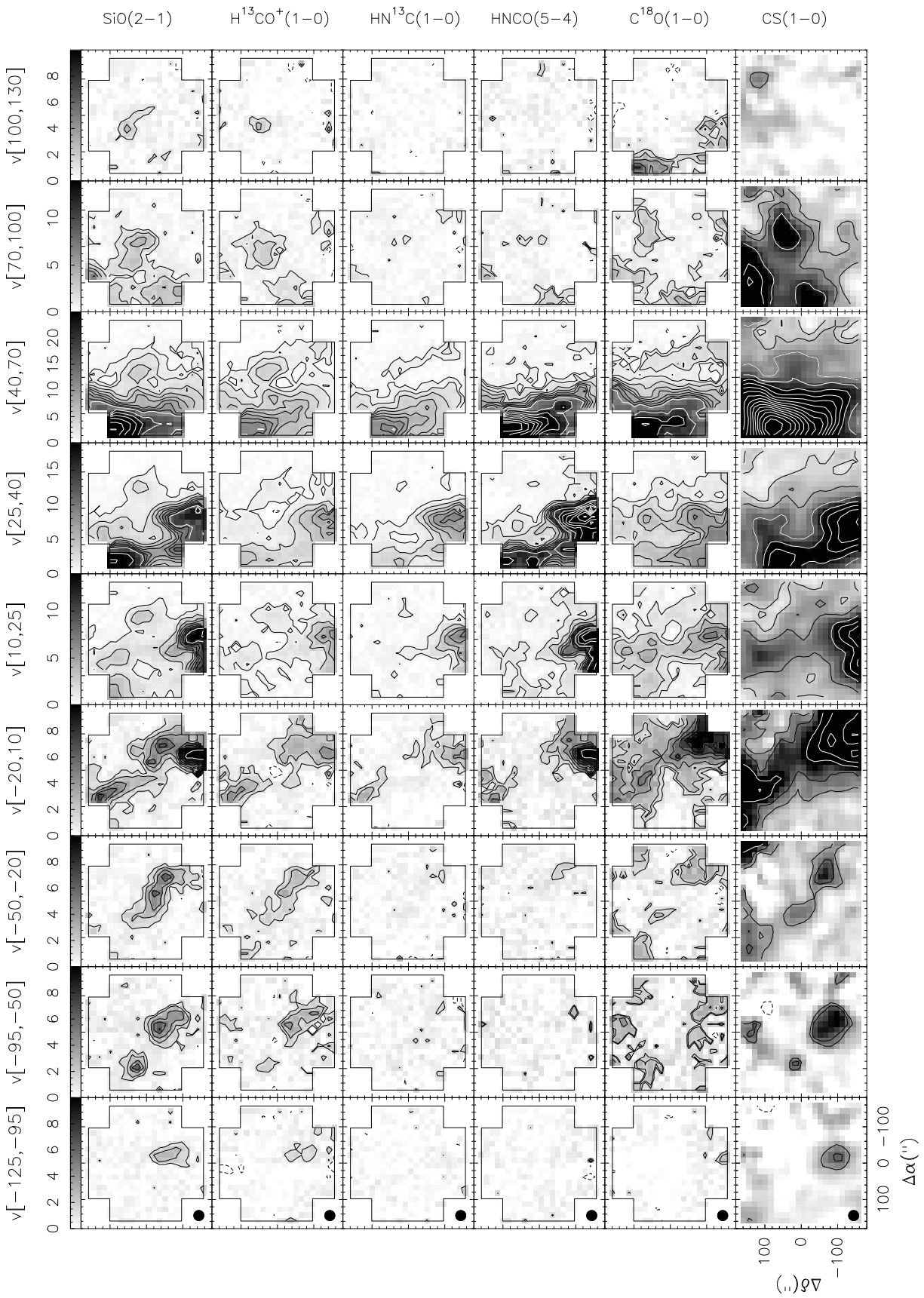

Fig. 2. Selected velocity-integrated maps for the different molecules observed at the Sgr A complex. Maps of the CS(1–0) line (Tsuboi et al. 1999) are displayed at the bottom. Each column corresponds to the same velocity range, indicated at the top of each column. The wedge at the top shows the intensity gray scale for each column. Contour levels for the integrated-velocity emission (in the T_A^* scale) of all the molecular lines, except CS(1–0), are -3σ (dashed contour), 3σ, from 2.0 to 12 in steps of 1.5 K km s^{-1} and from 12 in steps of 6 K km s^{-1}. Contour levels for the velocity-integrated CS(1–0) emission are -3σ (dashed contour), 3σ, and from 6 in steps of 6 K km s^{-1}. White contours are from 12 K km s^{-1}. The 3σ levels corresponding to the 15, 30, and 45 km s^{-1} wide velocity ranges are 0.7, 1.0, and 1.2 K km s^{-1} for the SiO(2–1), H^{13}CO$^+$(1–0), and HN^{13}C(1–0) maps; 1.0, 1.3, and 1.7 K km s^{-1} for the HNCO(5–4) and C^{18}O(1–0) maps; and 2.6, 3.7, and 4.5 K km s^{-1} for the CS(1–0) maps. The beam size (30″) is shown in the bottom-left corner of the first column panels. Sgr A* is the origin for the offset coordinates.

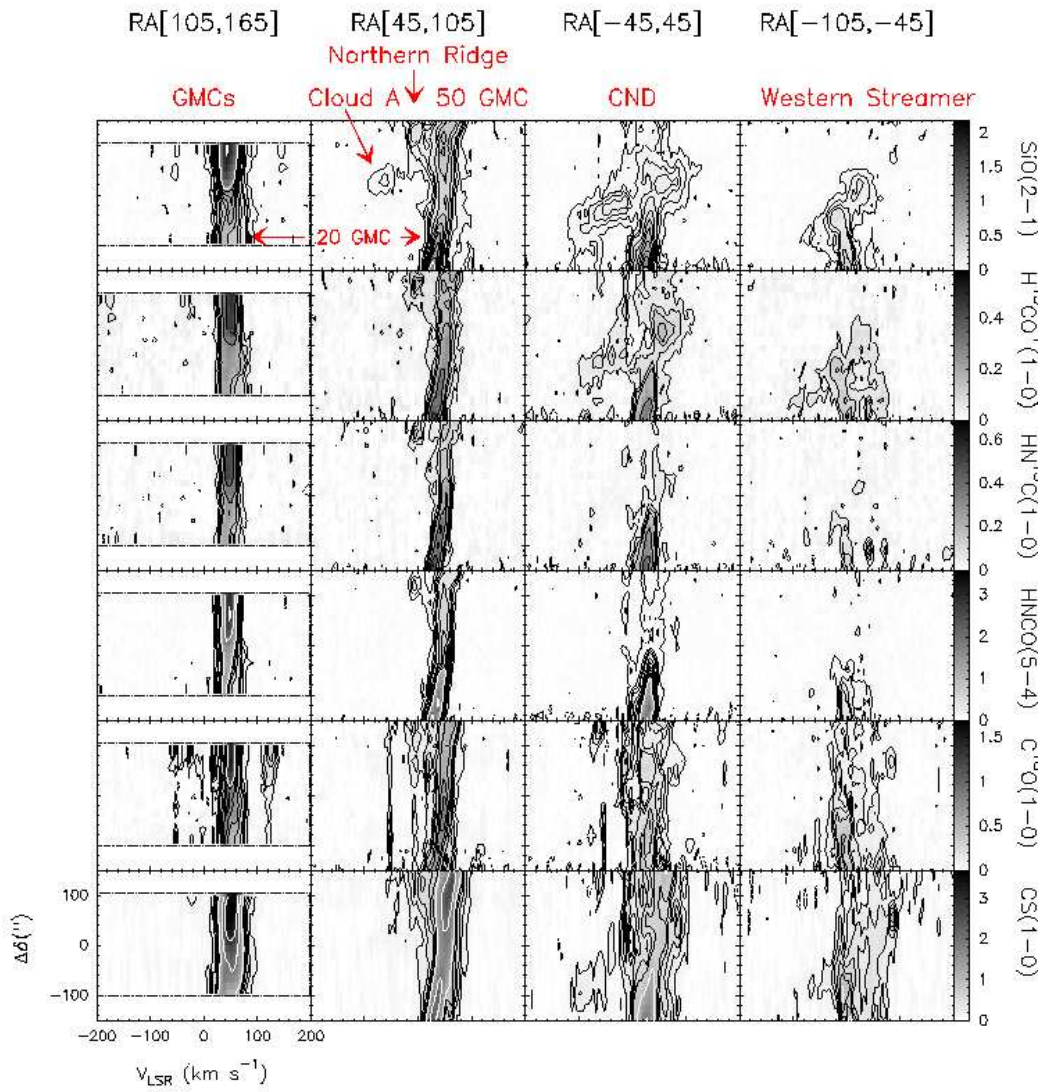

Fig. 3. Declination-velocity maps for the different molecules observed at the Sgr A complex. The $\Delta\delta$-v maps have been averaged in the right ascension ranges shown at the top of each column. Black contour levels are −3 (dashed contour), 3, 6, 9, and 12σ. The following contours are in steps of 9σ until 1 K. In the case of the CS(1–0) maps, black contour levels are −3 (dashed contour), 3, 6, 9, 12, and 15σ. The following contours are in steps of 12σ. White contours begin from 1 K and are in steps of 1 K. The 3σ levels corresponding to the 60″ and 90″ wide right ascension ranges are 0.04 and 0.03 K for the SiO(2–1), $H^{13}CO^+$(1–0), and $HN^{13}C$(1–0) maps; 0.06 and 0.04 K for the HNCO(5–4) and $C^{18}O$(1–0) maps; and 0.15 and 0.12 K for the CS(1–0) maps. The wedge on the right shows the intensity gray scale for each molecular line.

Sgr A East. The last maximum (−40″, −70″), which achieves its highest intensity in the velocity range [−50, −20] km s^{-1}, is also related to this SNR, as seems to border its southwestern region (labeled as Western St. South in Fig. 4). HCO^+(1–0) and HCN(1–0) emission has also been detected at this location by Wright et al. (2001). They attribute the emission to a continuation of the CND or to a high-velocity streamer. However, our data suggest that this emission could belong to the southernmost part of the Western Streamer. It appears in the declination-velocity maps (panel labeled RA= [−105″, −45″] in Fig. 3) as a coherent structure with a constant velocity gradient (~0.6 km s^{-1} arcsec^{-1} = 17 km s^{-1} pc^{-1}).

Between −50 and 10 km s^{-1}, the gas seems to connect the southwestern and northeastern regions, surrounding the Sgr A* position. However, this feature is very likely the result of the superposition of several previously identified molecular features. The emission closer to Sgr A* in projection comes from the eastern region of the CND (Jackson et al. 1993; Marshall et al. 1995). In previous HCN(1–0) single-dish observations, this part of the CND was absent because HCN emission was affected by self-absorption (Marshall et al. 1995). Even with the single-dish resolution, SiO emission perfectly traces the eastern region, although emission here is weaker than in the rest of the CND. Finally, the emission in this velocity range located in the northeastern quadrant ($\Delta\delta$ >40″) comes from the Northern Ridge and borders, in projection, the northern edge of the SNR Sgr A East. Emission from the western side ($\Delta\alpha$ < −40″) corresponds to the Western Streamer, whereas emission from the south comes from the northern part of the 20 km s^{-1} GMC, both features bordering the western and southwestern edges of this SNR (see

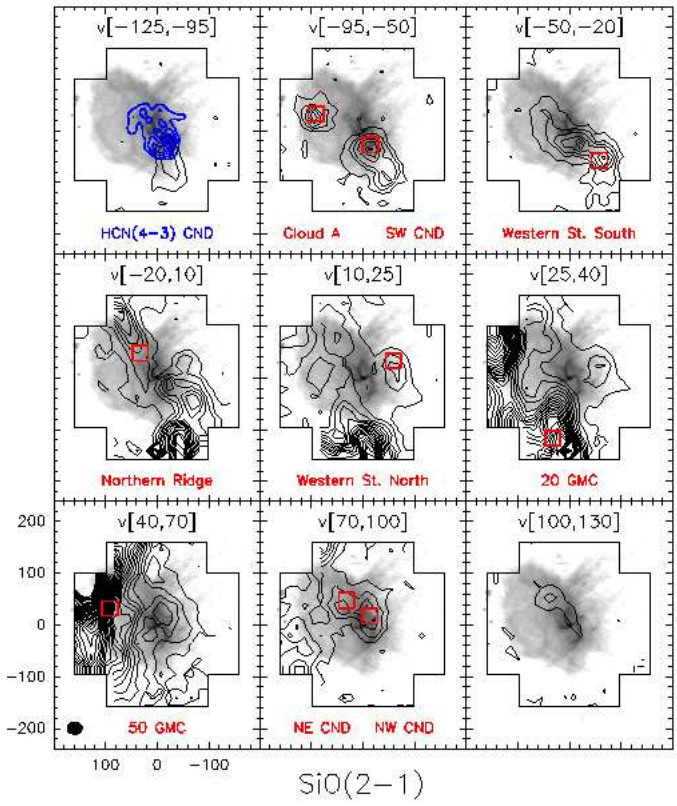

Fig. 4. Selected velocity-integrated maps of SiO(2–1) emission superimposed on the radio continuum image of Yusef-Zadeh & Morris (1987) at 6 cm in gray scale. We can appreciate the thermal feature Sgr A West, also known as the Minispiral, in the center of the image. The first two level contours are −0.7 0.7, −1.0 1.0, and −1.2 1.2 K km s^{-1} for integrated velocities 15, 30, and 45 km s^{-1}, respectively. Steps between levels are 1 K km s^{-1}. Open squares indicate the spatially integrated areas where spectra of Fig. 6 were obtained, which are associated with the main identified molecular features, whose names are indicated at the bottom of each corresponding panel. In the first panel, we also show the HCN(4–3) map of the CND of Montero-Castaño et al. (2009) smoothed to 15″ in thick blue contours.

Fig. 4).

In the velocity range [10, 40] km s^{-1}, we can see the northern region of the 20 km s^{-1} GMC (the Southern Streamer) and 50 km s^{-1} GMCs at east, together with the northern half of the Western Streamer, which peaks at (−60″, 20″), west of the CND (labeled as Western St. North in Fig. 4). At −5 km s^{-1}, the 20 km s^{-1} GMC begins to appear at the south. As the velocity increases, the molecular emission moves to the east to form other well-known features: the Molecular Ridge, a connection between the two most massive clouds of the Sgr A complex, the 20 km s^{-1} and 50 km s^{-1} GMCs. These three molecular features surround a cavity where the SiO(2–1) emission has low intensity between 20 to 35 km s^{-1}. At 70 km s^{-1}, the 50 km s^{-1} GMC finally disappears. The 50 km s^{-1} GMC is located on the eastern border of the SNR Sgr A East (see Fig. 4), whereas the molecular gas at the Southern Streamer could be affected by the interaction of two expanding shells: Sgr A East and G 359.92−0.09 (Coil & Ho 2000).

In the velocity range [40, 70] km s^{-1}, we can see another small cloud peaking at (−10″, 20″), just with a small offset east from the northern half of the Western Streamer. If we compare with the HCN(4–3) map of Montero-Castaño et al. (2009), we can conclude that this cloud could be part of the northwestern region of the CND (labeled as NW CND in Fig. 4). In the velocity range [70, 100] km s^{-1}, the emission from this cloud moves to the east (maximum at (40″, 35″)) showing a very good correlation with the northeastern region of the CND.

Finally, in the highest velocity range ([100, 130] km s^{-1}), the maximum of the emission is located at the north of the CND, at (35″, 55″). In summary, SiO(2–1) emission traces all previously identified molecular structures within the central 12×12 pc^2 region.

3.2. The $H^{13}CO^+$ (1–0) data cube.

The $H^{13}CO^+$(1–0) emission covers the same velocity range as the SiO(2–1) emission and nicely follows its morphology, except for the lower intensity of the $H^{13}CO^+$ emission and the absorption features that appear toward Sgr A*. Two absorption features are observed (Fig. A.2): One narrow feature centered at −52 km s^{-1} arising from the 3-kpc spiral arm (Lindqvist et al. 1995) and observed in emission in the $C^{18}O$(1–0) maps (see Sect. 3.5); and a wide feature arising from local gas with a likely contribution from gas within the nuclear region, since the SiO(2–1) emission also shows a decrease in its intensity across this velocity range.

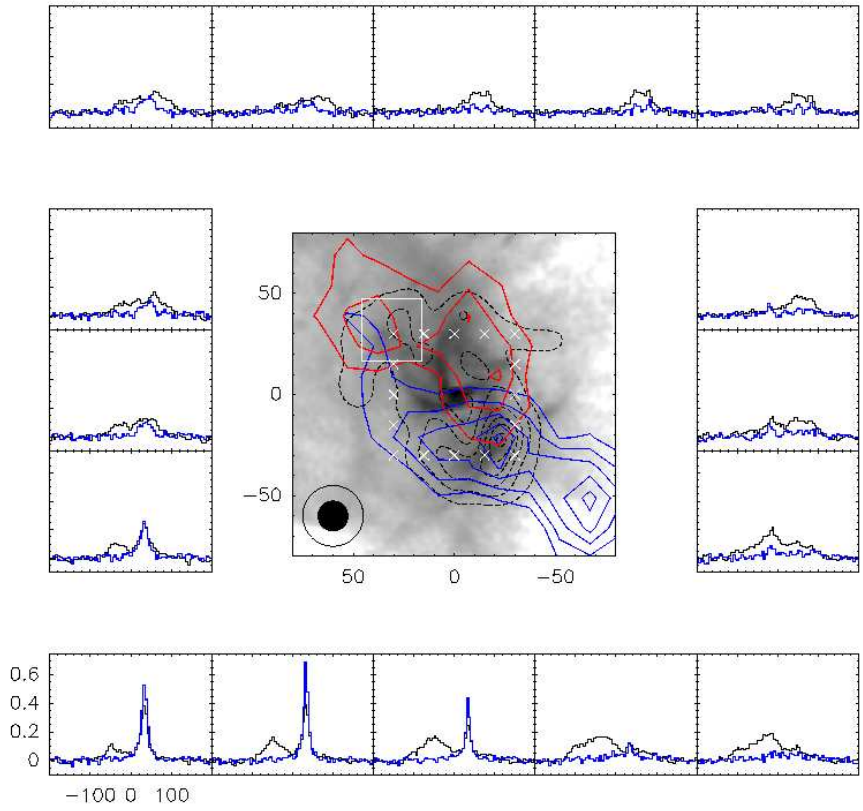

Fig. 5. Composition of the velocity-integrated maps of the SiO(2–1) emission at extreme velocities (velocity ranges between [−50, −20] km s^{-1} in thin blue contours and [70, 100] km s^{-1} in thick red ones), superimposed on the radio continuum image of Yusef-Zadeh & Morris (1987) at 6 cm in gray scale. Black dashed contours correspond to the HCN(4–3) interferometric map of the CND (Montero-Castaño et al. 2009) smoothed to 15″ resolution. The SiO(2–1) contour levels goes from 2 K km s^{-1} in steps of 1 K km s^{-1}. The white crosses indicate the centers of the 30″× 30″ squares where the shown spectra of SiO (black lines) and HNCO (thick blue lines) have been obtained. The beam size of the SiO(2–1) and HCN(4–3) emissions are shown as open and filled circles, respectively, in the bottom-left corner of the map.

3.3. The HN^{13}C(1–0) data cube.

The HN^{13}C(1–0) emission is weaker than that of H^{13}CO$^+$(1–0) and SiO(2–1). Most of its emission is concentrated in the GMCs and in the Molecular Ridge, going from −20 to 70 km s^{-1}. There is also low-intensity emission coming from the Northern Ridge visible in the velocity range [−20, 10] km s^{-1}; however, the eastern border of the CND is not traced by HN^{13}C. In contrast, its western side seems to be detected at the noise level in the velocity ranges between [40, 100] km s^{-1}. For the −82 km s^{-1} velocity-channel map (Fig. A.3), we can see very low-intensity emission coming from Cloud A, however, in the corresponding velocity-integrated map there is no trace of this cloud. At the velocity ranges between [10, 40] km s^{-1} there is low intensity emission from the northern half of the Western Streamer, as well as from its southern half in the velocity ranges between [−95, 10] km s^{-1}.

3.4. The HNCO(5–4) data cube.

This molecular line is the one that shows emission in the narrowest velocity range, only from −30 to 85 km s^{-1} in the velocity-channel maps (Fig. A.4). The HNCO emission is very intense only in the 20 and 50 km s^{-1} GMCs, and in the Molecular Ridge that connects both clouds. It is remarkable that HNCO(5−4) emission is the strongest of all the emission lines we have mapped, including C^{18}O. Outside these dense GMCs, the HNCO emission quickly drops. Between −25 and −5 km s^{-1}, we can appreciate the HNCO counterparts of the Northern Ridge and the 20 km s^{-1} GMC. However, as the molecular gas approaches the central position, it disappears. We do not detect the HNCO emission from Cloud A observed in other molecular lines at negative velocities. There is, however, a very low-level emission from the southern and northern parts of the Western Streamer in the velocity ranges between [−95, 40] km s^{-1}. Finally, the western side of the CND seems to be detected in the velocity range [70, 100] km s^{-1}.

3.5. The C^{18}O(1–0) data cube.

The C^{18}O(1–0) emission ranges from −80 to 95 km s^{-1} in the velocity-channel maps (Fig. A.5). However, only for velocities ≥ −30 km s^{-1} its emission seems to resemble the morphology observed in other molecular lines. We also find very low-intensity emission at around 170 km s^{-1} detectable in the spatially-averaged spectrum over the whole region, probably arising from the expanding molecular ring (Lindqvist et al. 1995), which also appears in the CS(1–0) averaged spectrum.

Between −80 to −55 km s^{-1}, the emission comes from the north, with no detected counterparts in the other molecules. Most of the narrow emission only seen in the −52 km s^{-1} channel map is foreground, arising from the 3-kpc spiral arm (Lindqvist et al. 1995). This feature is observed in absorption in the $H^{13}CO^+$(1–0) maps (see Sect. 3.2). The Northern Ridge, as well as gas surrounding Sgr A* with stronger emission at its western side, can be detected between −20 and 10 km s^{-1}. If we compare emission at these velocities with the SiO(2–1), we notice that the $C^{18}O$(1–0) emission is shifted toward the west. There is strong emission arising from the 20 and 50 km s^{-1} GMCs, and the Molecular Ridge, but we cannot clearly distinguish the emission from the northern part of the Western Streamer and Cloud A. At the highest velocities, there is $C^{18}O$(1–0) emission coming from the north, probably associated with the northwestern lobe of the CND, but more extended to the northwest than the SiO(2–1) and $H^{13}CO^+$(1–0) emission at these velocities. The same happens to the CS(1–0) emission.

From 100 to 130 km s^{-1}, we find low-intensity emission that resembles the morphology of the Molecular Ridge and the two GMCs of the Sgr A complex. This emission could come from $SO_2(17_{5,13}–18_{4,14})$ (Lindqvist et al. 1995) and/or $NH_2CHO(5_{1,4}–4_{1,3})$ (Jackson et al. 1984; Cummins et al. 1986). Cummins et al. (1986) found this line in their spectral survey of Sgr B2 and considered that the SO_2 line contributed with 10%. We also consider that the NH_2CHO line is the strongest one in this case. The upper-level energy of the NH_2CHO transition is lower than the upper-level energy of the SO_2 transition (19 K vs. 202 K). Moreover, the central velocity of the NH_2CHO line at the maximum of its emission is 45 km s^{-1}, whereas the central velocity of the SO_2 line is slightly redshifted (56 km s^{-1}) with respect to the lines from the other species ($\simeq$49 km s^{-1} on average). The origin of the NH_2CHO molecule could be related to the HNCO origin. Bisschop et al. (2007) find a strong correlation between both species in their survey of molecules suspected to be produced by the grain surface chemistry at several selected high-mass young stellar objects. This correlation suggests that HNCO and NH_2CHO molecules share a similar formation mechanism, i.e. grain chemistry. The NH_2CHO emission appears to be stronger in the 50 km s^{-1} GMC, a molecular cloud affected by shocks driven by the SNR Sgr A East, that could eject this molecule to the gas phase. In the following, we do not discuss this emission since it is rather weak, and it is only significantly detected toward the 50 km s^{-1} GMC.

4. Physical conditions of the gas and column density estimates.

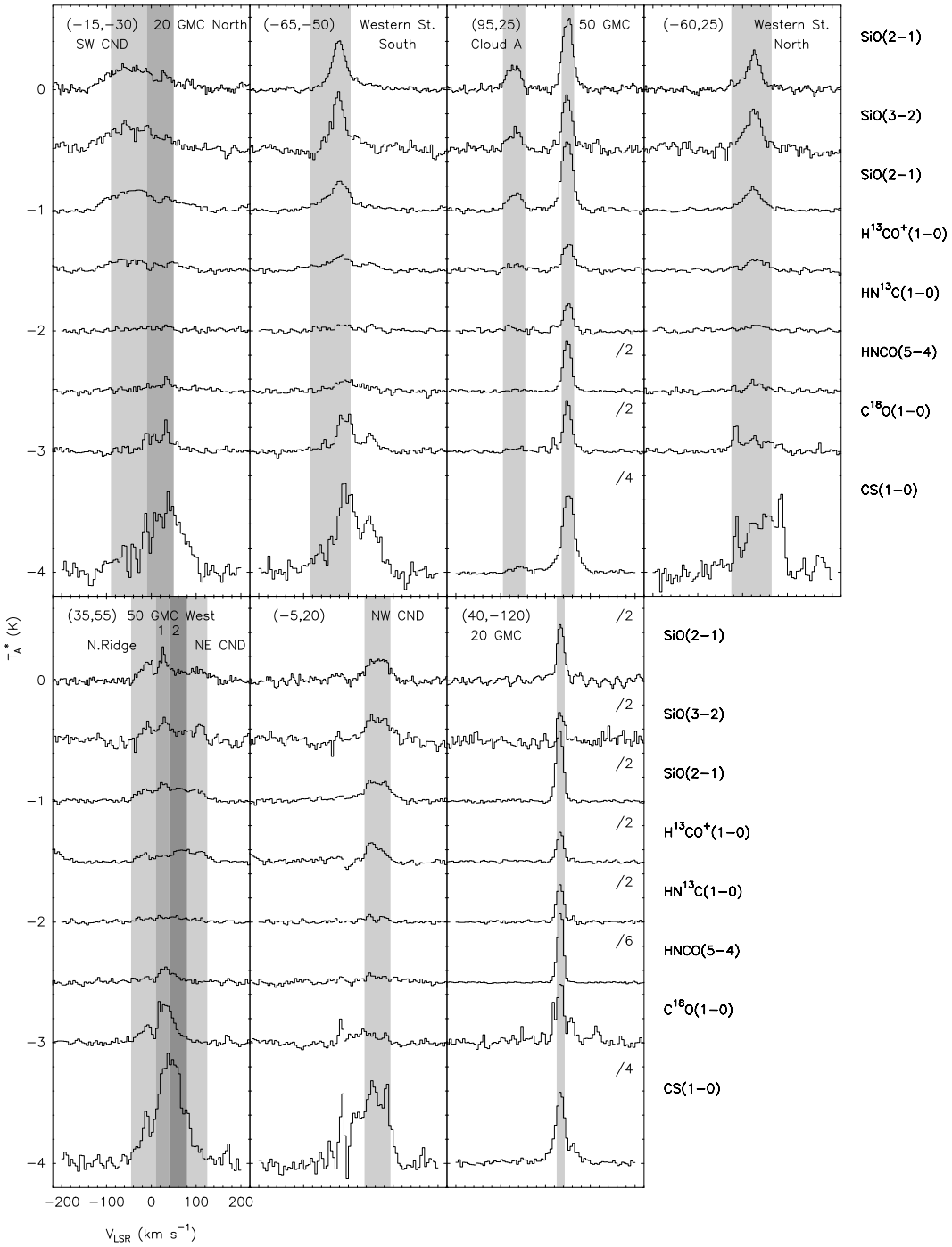

Fig. 6. Spectra of the observed transitions taken at 7 selected positions (marked with open squares in Fig. 4). The upper SiO(2–1) and the SiO(3–2) spectra were observed simultaneously at the offset positions respect to Sgr A* (in arcseconds) shown in the upper-left corner of each panel. The other SiO(2–1) spectra, together with the other molecular line spectra, were extracted from their respective data cubes from squares of area 30″× 30″. Shadowed areas represent the selected velocity ranges where integrated intensities of the observed molecular lines were obtained, labeled with the names of their associated features. The intensity of some transitions has been divided by a factor shown in the upper-right corner of the corresponding spectrum.

Table 2. Integrated intensities in selected velocity ranges.

Offset (")	Component	Δv (km s^{-1})	$\int T_A^* dv$ (K km s^{-1})					
			SiO(2−1)	$H^{13}CO^+$(1−0)	$HN^{13}C$(1−0)	HNCO(5−4)	CS(1−0)	$C^{18}O$(1−0)
(−15, −30)	SW CND	[−90,−10]	11.79±0.24	5.91±0.24	1.19±0.24	1.2±0.3	12±1	2.4±0.3
	20 GMC North	[−10, 50]	5.47±0.21	2.49±0.21	1.62±0.21	3.26±0.23	26.1±0.8	7.15±0.23
(−65, −50)	Western St. South	[−85, 5]	12.32±0.23	6.70±0.23	2.61±0.23	3.6±0.3	28.8±1.0	10.9±0.3
(95, 25)	Cloud A	[−95, −45]	4.99±0.22	1.78±0.22	0.95±0.22	≤ 0.8	5.3±0.6	2.0±0.3
	50 GMC	[36, 64]	13.48±0.17	5.04±0.17	4.71±0.17	16.73±0.20	61.9±0.5	16.16±0.20
(−60, 25)	Western St. North	[−25, 65]	8.79±0.23	4.82±0.23	2.48±0.23	3.1±0.3	30.6±1.0	8.3±0.3
(35, 55)	Northern Ridge	[−45, 10]	4.12±0.18	2.15±0.18	1.28±0.18	1.55±0.25	13.1±0.7	4.40±0.25
	50 GMC West I	[10, 40]	3.81±0.14	1.44±0.14	1.14±0.14	2.86±0.18	21.3±0.5	8.20±0.18
	50 GMC West II	[40, 80]	4.03±0.16	3.33±0.16	1.45±0.16	1.83±0.21	26.7±0.6	4.93±0.21
	NE CND	[80, 125]	3.60±0.17	3.44±0.17	0.75±0.17	≤ 0.7	7.0±0.6	≤ 0.7
(−5, 20)	NW CND	[36, 94]	8.38±0.20	6.02±0.20	1.85±0.20	2.5±0.3	31.5±0.6	3.2±0.3
(40, −120)	20 GMC	[25, 43]	17.07±0.15	7.06±0.15	9.06±0.15	47.84±0.24	36.8±0.5	7.32±0.24

Note.— When molecular lines are undetected (<3σ), we use the upper limit to the integrated intensity derived from the spectrum rms noise.

Table 3. Derived physical conditions of the gas and column densities in selected positions.

Offset (")	Component	Δv (km s^{-1})	τ_{SiO}	T_{ex}^{SiO} (K)	n_{H_2} (× 10^5 cm^{-3})	N_{SiO}	$N_{H^{13}CO^+}$	$N_{HN^{13}C}$	N_{HNCO}	N_{CS}	$N_{C^{18}O}$
						(× 10^{13} cm^{-2})					(× 10^{16} cm^{-2})
(−15, −30)	SW CND	[−90,−10]	0.03	9	3	1.9	0.5	0.17	1.4	15	0.6
	20 GMC North	[−10, 50]	0.020	9	4	0.8	0.25	0.23	4	30	1.9
(−65, −50)	Western St. South	[−85, 5]	0.03	8	3	1.9	0.6	0.4	4	30	3
(95, 25)	Cloud A	[−95, −45]	0.03	6	1.8	0.8	0.13	0.15	≤ 0.8	5	0.5
	50 GMC	[36, 64]	0.15	6	1.5	2.4	0.4	0.8	16	60	4
(−60, 25)	Western St. North	[−25, 65]	0.017	12	5	1.4	0.5	0.4	4	50	2.2
(35, 55)	Northern Ridge	[−45, 10]	0.022	6	1.5	0.7	0.16	0.22	1.5	11	1.1
	50 GMC West I	[10, 40]	0.04	7	2.4	0.6	0.12	0.17	3	22	2.1
	50 GMC West II	[40, 80]	0.014	8	3	0.6	0.3	0.21	2.1	30	0.9
	NE CND	[80, 125]	0.012	10	5	0.6	0.4	0.12	≤ 0.8	10	≤0.17
(−5, 20)	NW CND	[36, 94]	0.03	10	4	1.4	0.6	0.3	3	40	0.8
(40, −120)	20 GMC	[25, 43]	0.5	4	0.4	6	0.6	3	50	25	1.5

To estimate the column densities of the observed molecules, we selected several positions located at maxima of the SiO(2–1) emission. The spectra toward these positions can be seen in Fig. 6. These spectra show at least 9 different velocity components that can be fitted to Gaussian profiles, however, other components cannot be fitted. Moreover, in some cases it is not possible to separate contributions from the different molecular features that appear at the same position but in different velocity ranges using Gaussian profiles. Therefore, we derived the column densities of the observed molecules from integrated intensities in selected velocity ranges (see Table 2). These selected velocity ranges are shown as shadowed areas in Fig. 6, labeled with their associated molecular feature, and the location of most of these components in the α-δ-v space is indicated in Fig. 4. We note that the components 20 GMC North and 50 GMC West are very likely contaminated with molecular gas from the CND.

The procedure used to derive the column densities is the following. We constrained combinations of the pair kinetic temperature (T_k) and volume density (n_{H_2}), together with the SiO column density (N_{SiO}), by matching the two observed transitions of SiO (two upper spectra in each panel of Fig. 6) using a large velocity gradient (LVG) excitation code. We explored a range of T_k from 30 to 200 K, as derived from ammonia inversion lines by Hüttemeister et al. (1993) in several clouds of the GC and by Herrnstein & Ho (2005) in the central 10–20 pc region. Both studies conclude that molecular clouds in the GC can be roughly characterized by a two-temperature gas distribution in which 75% of the column density comes from cool gas (~25 K) and the remaining 25% from hot gas (~200 K). Furthermore, Rodríguez-Fernández et al. (2001) find, from observations of S(0) to S(5) H_2 pure-rotational lines toward several molecular clouds of the GC, that warm gas (~150 K) represents the ~30% of the gas traced by low-J CO isotopes. Then, we modeled the intensity of the other molecular lines (of HNCO(5–4) and $C^{18}O$(1–0) lines using the RADEX LVG excitation code; van der Tak et al. 2007) with the previously derived physical condition pairs (T_k and n_{H_2}), in order to obtain their column densities. As all the observed transitions, except $C^{18}O$(1–0), have similar dipole moments (from 1.60 to 3.89 D), we can assume that all transitions sample the same molecular gas (i.e., gas with similar physical conditions). However, for the $C^{18}O$(1–0) line (0.11 D), the derived column density values should be taken with caution.

In Table 3 we present the results of this analysis for a T_k of 50 K. Raising the kinetic temperature by a factor of 4 has almost no effect on the excitation temperature and column density of SiO, but it decreases the volume density by a factor of ~3, except for the 20 km s^{-1} GMC, where the volume density decreases by a factor of 4. The derived n_{H_2} values at T_k =50 K are very similar for all the gas components, (1.5–5) $\times 10^5$ cm^{-3}, except for the 20 km s^{-1} GMC, where the volume density shows the minimum value (~4×10^4 cm^{-3}). The SiO emission is optically thin, showing maximun optical depths of 0.5 toward the 20 and ~0.15 toward 50 km s^{-1} GMCs. The SiO transitions are subthermally excited, with T_{ex} ranging from 4 K at the 20 km s^{-1} GMC to 12 K in the northern part of the Western Streamer, in agreement with previous estimates in the GC (Hüttemeister et al. 1998). The SiO column densities, 0.6–6 $\times 10^{13}$ cm^{-2}, show less variation than the HNCO column densities, ≤0.8–50 $\times 10^{13}$ cm^{-2}.

HNCO column density presents the strongest contrast, with a difference of a factor of ≥60 between Cloud A and the 20 km s^{-1} GMC. HNCO excitation temperatures show larger variations, depending on the volume density. Except for the 20 km s^{-1} GMC, where the excitation temperature ranges between 9 and 15 K, the HNCO excitation temperatures are in general ≥40 K. These values agree with the rotational temperatures derived by Martín et al. (2008) using the rotational diagrams obtained from several HNCO transitions. They obtained T_{rot} =35±12 K and T_{rot} =13.6±0.2 K in their positions (−30″, −30″) and (−15″, −215″) relative to Sgr A*, respectively. The first position almost coincides with our (−15″, −30″) position, whereas the second is located at the core of the 50 km s^{-1} GMC. Therefore, our results share a similar trend, that is, the lowest HNCO excitation temperatures are shown toward the cores of the GMCs. HNCO column densities show almost no variation for the different T_k and n_{H_2} pair values derived from the SiO transitions. The largest variation is found for the 20 km s^{-1} GMC position with only a factor 1.6 more at 200 K than at 50 K. The HNCO emission is optically thin in all the cases (≤0.2).

In general, uncertainties in the column densities due to calibration (assuming a conservative 20%), and rms noise in the spectra are lower than a factor of 2. As for HNCO and SiO, changing the kinetic temperature from 50 to 200 K has almost no effect on the $H^{13}CO^+$, $HN^{13}C$, and CS column densities. The largest variation is also found for the 20 km s^{-1} GMC position, with a factor of 1.2 and around 1.7 larger at 200 K than at 50 K for CS and the other species. The $C^{18}O$ column densities present larger differences with kinetic temperature, with factors up to 3. This higher sensitivity to volume density is expected, as $C^{18}O$ is the molecule with the lowest critical density among the species studied in this paper. Therefore, we conclude that our column density estimates for SiO, $H^{13}CO^+$, $HN^{13}C$, HNCO, and CS could present uncertainties of up to a factor of 2.

5. Integrated intensity maps and fractional abundances.

To derive the fractional abundances of the observed species, we need to evaluate the hydrogen column density at the selected positions. As mentioned before, $C^{18}O$ is not the best tracer because it samples molecular gas biased toward low hydrogen volume densities, and it is strongly affected by gas along the LOS toward the GC. Alternatively, CS is more likely arising from the same high-density molecular gas as the other observed molecules, and it is moderately affected by any particular chemistry taking place at the central 12 parsecs. It is only marginally enhanced in UV (Goicoechea et al. 2006; Martín et al. 2008) and shock-dominated environments (Requena-Torres et al. 2006). However, the drawback is that CS(1–0) could be moderately affected by opacity.

To elucidate the effects of CS opacity in our estimation of the fractional abundances, we made integrated intensity ratio maps relative to the CS(1–0) emission (Fig. 7). Additionally, we present intensity ratio maps made in the same selected velocity ranges as Fig. 2 (Fig. B.1) in the online version. As we can see in Figs. 7 and B.1, the $C^{18}O$(1–0)/CS(1–0) ratio is rather uniform. The highest values are found at negative velocities, very likely associated with foreground molecular gas, and the lowest values at positive velocities associated with the northern part of the CND. These lower values indicate that the molecular gas is denser in the CND than in the surrounding GMCs (see Table 3). Therefore, CS(1–0) emission does not seem to be severely affected by optical depth effects.

Using CS as a high-density molecular gas tracer and assuming a CS fractional abundance of $X_{CS} = N_{CS}/N_{H_2}$=10^{-8}

Table 4. Fractional abundances.

Offset (")	Component	X_{SiO}	$X_{H^{13}CO^+}$	$X_{HN^{13}C}$	X_{HNCO}	$X_{C^{18}O}$
			($\times10^{-9}$)			($\times10^{-7}$)
(−15, −30)	SW CND	1.3	0.4	0.12	1.0	4
	20 GMC North	0.24	0.07	0.07	1.1	5
(−65, −50)	Western St. South	0.6	0.18	0.11	1.2	8
(95, 25)	Cloud A	1.8	0.3	0.3	≤1.7	11
	50 GMC	0.4	0.06	0.14	3	7
(−60, 25)	Western St. North	0.3	0.11	0.08	0.9	5
(35, 55)	Northern Ridge	0.6	0.15	0.20	1.4	10
	50 GMC West I	0.3	0.05	0.08	1.4	9
	50 GMC West II	0.20	0.09	0.07	0.7	3
	NE CND	0.6	0.4	0.12	≤0.8	≤1.8
(−5, 20)	NW CND	0.3	0.14	0.06	0.7	1.9
(40, −120)	20 GMC	2.4	0.25	1.3	19	6

Note.— Fractional abundances with respect to H_2, derived from the CS column density assuming $X_{CS}=10^{-8}$ for the GC.

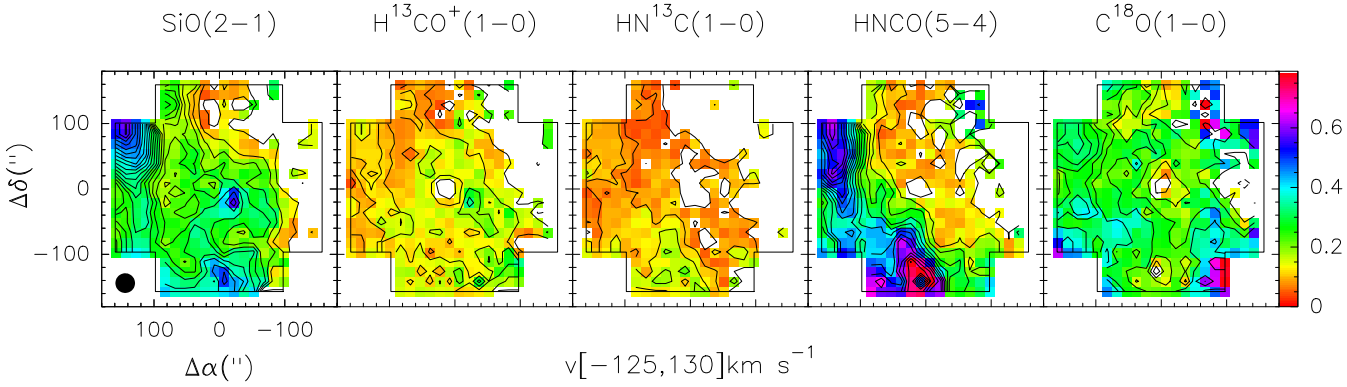

Fig. 7. X/CS(1–0) intensity ratios in the full velocity range shown at the bottom of the figure. X stands for SiO(2–1), $H^{13}CO^+$(1–0), $HN^{13}C$(1–0), HNCO(5–4), and $C^{18}O$(1–0), whose emission is shown in contour levels. Intensity ratios have been derived considering only pixels with emission above the 3σ level. The wedge to the right shows the color scale of the intensity ratios. Contour levels are -3σ (dashed contour) and from 3σ in steps of 4σ (3.9 and 5.2 K km s^{-1} for SiO/$H^{13}CO^+$/$HN^{13}C$ and HNCO/$C^{18}O$ ratios, respectively).

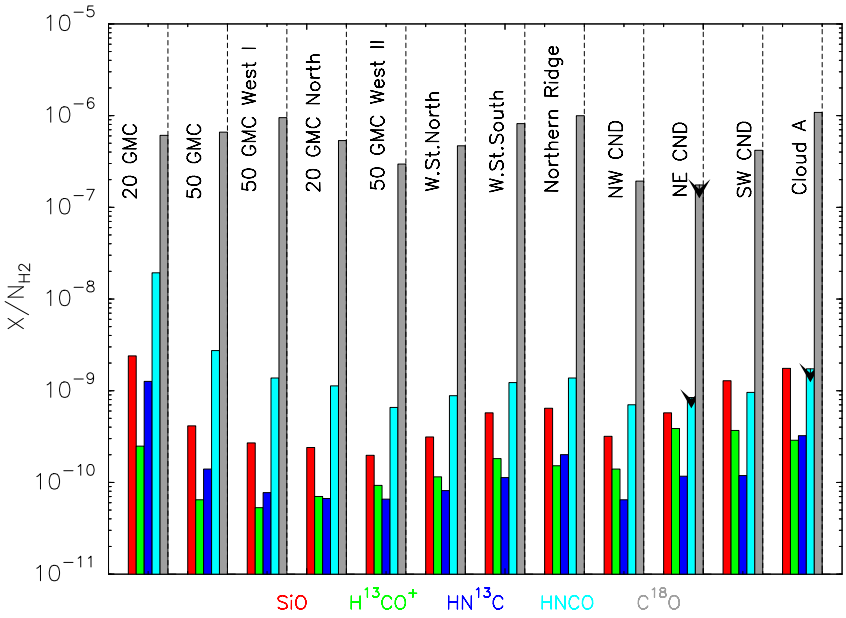

Fig. 8. Histogram with the fractional abundances shown in Table 4. X stands for SiO (red), $H^{13}CO^+$ (green), $HN^{13}C$ (blue), HNCO (cyan), and $C^{18}O$ (gray), from left to right for every source.

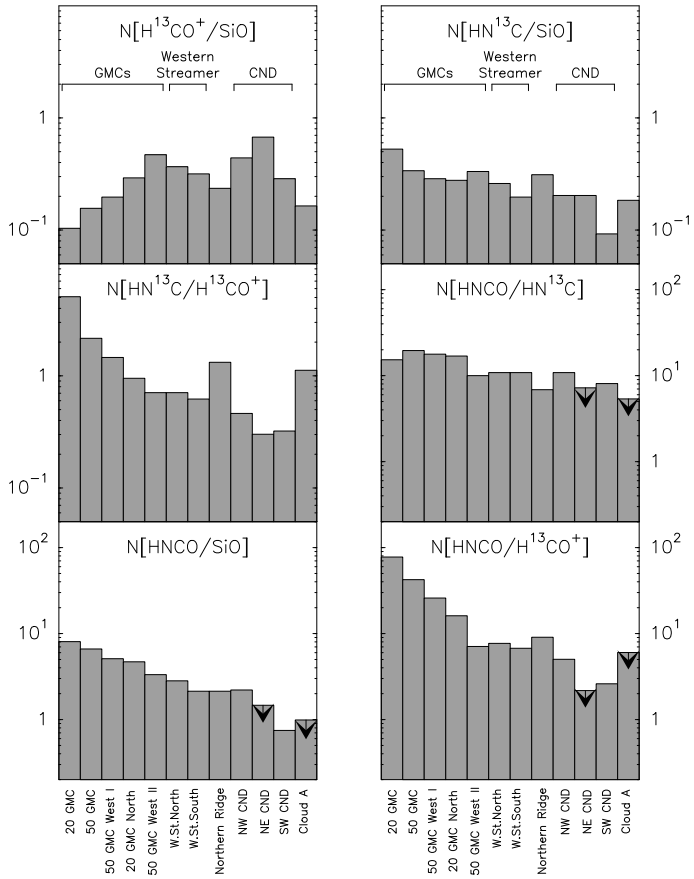

Fig. 9. Histogram with ratios between column densities shown in Table 3.

(Irvine et al. 1987) for the GC, we derive hydrogen column densities between 0.5–6×10^{22} cm^{-2}. As already mentioned, Table 4 and Fig. 8 show that $C^{18}O$ is the molecule that presents the smallest variation in its fractional abundance, with only a difference of a factor of 6. On the other hand, HNCO is the molecule that presents the largest variation of a factor of 28, with the highest values toward the cores of the GMCs, and the lowest ones toward the positions associated with the CND. Conversely, SiO presents a smaller variation of a factor of 12, and does not follow the trend observed in HNCO. SiO fractional abundance is high at the cores of the GMCs, as well as in the positions of the CND. A similar behavior to HNCO follows $HN^{13}C$ (a factor of 20). $HN^{13}C$ seems to be anticorrelated with $H^{13}CO^+$, which shows the smallest variation in its fractional abundance after $C^{18}O$ (a factor of 7).

The same trends can be seen in the integrated intensity ratio maps. The highest SiO(2–1)/CS(1–0) ratios and SiO fractional abundances are reached at the southwest lobe of the CND and Cloud A, only comparable to the ratio found at the GMCs. The gas components associated with the whole CND, the Western Streamer, and the Northern Ridge also present higher ratios than the surrounding gas (see Fig. B.1 in the online version). The $H^{13}CO^+$(1–0)/CS(1–0) ratio seems to follow similar behavior to the SiO(2–1)/CS(1–0) ratio, except for the gas components associated with the GMCs. The $HN^{13}C$(1–0)/CS(1–0) and HNCO(5–4)/CS(1–0) ratios shares a similar behavior, reaching the maximum values of their ratios and abundances at the 20 km s^{-1} GMC, and decreasing toward the nuclear region.

Figure 9 presents histograms with the ratios between column densities of SiO, $H^{13}CO^+$, $HN^{13}C$, and HNCO toward selected positions. Sources have been ordered from left to right according to the HNCO/SiO column density ratio. There seems to be a relation between the HNCO/SiO ratio and the distance to the nuclear region. All sources related with the GMCs are grouped with the highest ratios, the Western Streamer and Northern Ridge present intermediate values, whereas ratios toward the CND and Cloud A show the lowest values. Similar trends present all the other ratios, except for the $H^{13}CO^+$/SiO column density ratio. The HNCO/$HN^{13}C$ ratio is rather uniform with only a factor of 4 difference between the maximum and minimum values. Variations in the $HN^{13}C$/SiO, $H^{13}CO^+$/SiO, and HNCO/SiO ratios are within factors 6, 7, and 8, respectively, whereas variations in the $HN^{13}C/H^{13}CO^+$ and HNCO/$H^{13}CO^+$ ratios are the greatest, with values of 17 and 40, respectively.

In summary, we can group the observed species in those whose abundances decrease (HNCO and $HN^{13}C$) and those whose abundances are constant or enhanced (SiO and $H^{13}CO^+$) toward the nuclear region.

6. Discussion.

Table 5. Fractional abundances.

Source		X_{SiO}	$X_{H^{13}CO^+}$	$X_{HN^{13}C}$	X_{HNCO} ($\times10^{-9}$)	X_{CS}	$X_{H^{13}CN}$	N_{H_2} ($\times10^{22}$ cm^{-2})	Chemistry	References
SW CND		1.3	0.4	0.12	1.0	10	...	1.5	PDR+Shock	
20 GMC		2.4	0.25	1.3	19	10	...	2.5	Shock	
Galactic sources										
Orion Bar	(20″, −20″)	0.03	0.05	... / 0.014	≤0.015	23	... / 0.07	6.5	PDR	1, 2
	(60″, −60″)	...	... / 0.08	... / 0.08	≤0.3	5	... / 0.04	0.3		
IC443−G		0.8	≤0.1 / 0.05	... / 0.015	...	3	... / 0.12	1.2	Shock	3
Orion KL−Plateau		22	...	...	7	11	...	21	Shock	4, 5, 6
Orion KL−Hot Core		3	...	...	14	50	...	42	Hot Core	
TMC−1		≤6×10^{-4}	0.18	0.20	1.5	4	0.17	1	Ion-molecule	7
Extragalactic sources										
NGC 253		0.13	0.04	0.025	1.6	6	0.13	6.7	SB	8
NGC 4945		≤0.13	0.10	0.3	4	4	0.20	6.4	AGN+SB ring	8, 9
M 82	Southwest	≤0.12	0.12	...	≤9	2.3	...	3.8	Evolved SB	8, 10, 11
	Center	...	... / 0.06	≤0.3 / 0.04	≤9	7	≤0.24 / 0.09	3.8		
	Northeast	...	...	...	≤0.12	4	...	2.4		
IC 342	Center	...	... / 0.04	... /0.06	3	4	... / 0.14	1.3	Normal−nucleus	
	North	≤0.9	0.4	...	5	6	≤1.1	1.1	Normal−arm	
IC 342 (interf.)	A	0.16	0.12	... / 0.08	≤4	... / (30–80)	... / 0.22	2.3	Normal−nucleus	12, 13, 14
	D	0.4	0.06	... / 0.04	5	... / ≤(8–23)	... / 0.14	1.7	Normal−arm	
	D′	...	...	... / 0.03	8	... / ≤(6–16)	...	2.0		

References.—(1) Jansen et al. (1995); (2) Schilke et al. (2001); (3) van Dishoeck et al. (1993); (4) Marcelino et al. (2009); (5) Tercero et al. (2010); (6) Tercero et al., in prep.; (7) Marcelino (2007); (8) Martín et al. (2006); (9) Wang et al. (2004); (10) Martín et al. (2009a); (11) Bayet et al. (2009); (12) Downes et al. (1992); (13) Meier & Turner (2005); (14) Usero et al. (2006).

Notes.— *Galactic sources*: The second value of the $H^{13}CO^+$, $HN^{13}C$, and $H^{13}CN$ abundances has been derived from the main isotope assuming a $^{12}C/^{13}C$ isotopic ratio of 65 for the Orion Bar and the SNR IC443−G. *Extragalactic sources*: a source size of 20″ (Martín et al. 2006; Wang et al. 2004) has been assumed in our column density estimations of M 82 and IC 342 from single-dish observations, as well as optically thin emission and the LTE approximation. For that purpose, integrated intensities have been taken from the compilation made by Martín et al. (2006) plus additional data taken from Martín et al. (2009a) and Bayet et al. (2009). The second values of the $H^{13}CO^+$, $HN^{13}C$, and $H^{13}CN$ abundances have been derived from the main isotopes assuming $^{12}C/^{13}C\simeq 40$ (Henkel et al. 1998). Interferometric IC 342 abundances have been derived from the parameters of the line profiles taken from Usero et al. (2006), Meier & Turner (2005), and Downes et al. (1992), assuming a source size of 6″, optically thin emission, and the LTE approximation. CS abundance has been derived from $C^{34}S$ assuming $^{32}S/^{34}S\sim$ 8–23 (Meier & Turner 2005).

In this section, we discuss the most outstanding chemical differences found in our data in the context of the two main mechanisms considered to be the main drivers of the chemistry and the heating of the central region: shocks and UV radiation (see Sect. 1). To establish the dominant chemistry for the GC clouds from the observational point of view, we have selected several sources that are well-known prototypes of the different kinds of chemistry in the Milky Way and in nearby galaxies (see Table 5). A brief description of the physical conditions of these prototypical sources is given before the discussion. To avoid uncertainties associated with the different ways in which the fractional abundances were calculated for the prototypical sources, we do not compare fractional abundances, but rather their ratios (see Table 6). From all the sources in the central 12 pc where we have derived abundances, we have selected the SW CND and 20 GMC as the most representative positions for the chemistry in this region. We find a difference of one order of magnitude between the HNCO/CS and $HN^{13}C$/CS abundance ratios toward both sources, whereas the SiO/CS and $H^{13}CO^+$/CS ratios show very similar values.

Finally, once we had defined the dominant chemistry drivers for each particular species, we used the effects that UV radiation produces on the molecular gas to establish the location of the different molecular components relative to the Central cluster.

6.1. Prototypical sources.

As Galactic prototypical sources, we selected a cold dark cloud, a photo-dissociated region (PDR), molecular clouds interacting with an SNR and molecular outflows, and two hot cores.

TMC-1 is one of the best-studied quiescent dark clouds, with temperatures around 10 K and densities of a few 10^4 cm^{-3}. Due to the lack of internal heating sources and shocks, dark clouds are the best places to study gas-phase chemistry driven by ion-neutral reactions.

As PDR, we have selected the OMC−1 ridge. The UV radiation is provided mostly by the Trapezium stars, which are located at 0.25 pc from the PDR. The mean kinetic temperature in the molecular layers of this PDR is around 85 K with 90% of the molecular gas in a homogeneous layer of density of 10^4 cm s^{-1} and the remaining material concentrated in high-density clumps of $\sim 10^6$ cm s^{-1} (Hogerheijde et al. 1995). The UV radiation flux in the Orion PDR seems to be quite similar to that of the inner edge of the CND, with $G_0 \sim 10^5$ (in units of the Habing field; Burton et al. 1990).

To test shock chemistry, we use clump G in the SNR IC443, where shocks occur nearly perpendicular to the LOS. Densities and temperatures of the shocked gas are 10^5–3×10^6 cm^{-3} and 80–200 K, respectively (van Dishoeck et al. 1993). Unfortunately, HNCO has not been studied toward molecular clouds affected by SNRs. However, HNCO among other species, have been observed toward the closest high-mass star-forming region in our Galaxy, the Orion KL cloud (Tercero et al. 2010). Single-dish line surveys find several spectral components within a telescope beam. One of these components, known as the *plateau*, presents a chemistry dominated by shocks driven by molecular outflows. The physical conditions of this component is characterized by temperatures and densities around 100–150 K and $\sim 10^5$ cm^{-3}, respectively (see the introduction of Persson et al. 2007).

As prototypical hot cores, Sgr B2(N) and the hot core component of Orion KL were selected. The first one is the most prominent hot core of the Sgr B2 GMC complex located at the GC. It presents densities as high as 10^7 cm^{-3} and temperatures that go from 20 K to up to 80 K averaged over a region of 1 pc, being even higher (150 K) on smaller scales (see Nummelin et al. 2000). The Orion hot core is a warm star-forming region internally heated by one or more young massive protostars. It contains very dense clumps ($\sim 10^7$ cm^{-3}) and presents temperatures between 165–400 K (see the introduction of Persson et al. 2007).

On the other hand, as extragalactic prototypical sources, we selected three starburst nuclei in different evolutionary stages (NGC 253, M 82, and NGC 4945), and a normal spiral galaxy more similar to the Milky Way (IC 342). When one compares GC abundances with those of extragalactic nuclei measured with single-dish telescopes, it has to be taken into account that single-dish measurements represent average values over regions of hundreds of parsecs that contains a large number of GMCs. At best, interferometer observations are able to provide average abundances over individual GMCs ($\sim$ 50 pc).

6.2. SiO chemistry.

SiO is one of the best tracers of energetic mechanical phenomena in the ISM, with fractional abundances that changes by 5 orders of magnitude in dark clouds $\sim 10^{-12}$ to regions associated with shocks $\sim 10^{-7}$ (Martín-Pintado et al. 1992; Jiménez-Serra et al. 2005). Indeed, the most outstanding difference between TMC-1 and the central 12-pc sources is the SiO/CS abundance ratio, since it is more than 2–3 orders of magnitude larger in the SW CND and the 20 GMC than in cold clouds. The reason for this huge variation is the depletion of SiO onto grains in quiescent clouds. Only when energetic mechanisms destroy or erode dust grains does SiO appear with significant abundance in the gas phase.

The widespread SiO emission in the GC, with typical abundances of $\sim 10^{-9}$ (Martín-Pintado et al. 1997), has led to the conclusion that large-scale shocks must be at work in the GC. However, there are other energetic mechanisms, apart from shocks, that might enhance SiO abundances. It has been proposed that high-energetic phenomena, like X-rays as observed by the 6.4 keV Fe line, enhance the SiO abundance (Martín-Pintado et al. 2000; Amo-Baladrón et al. 2009) in the GC over the averaged value. But, the 20 and 50 km s^{-1} GMCs do not seem to present an enhancement of the 6.4 keV Fe line, which would indicate a recent interaction of molecular gas with X-rays.

Another energetic mechanism that could enhance SiO abundance in PDRs is the desorption of grain mantles by UV-photons, as Schilke et al. (2001) have shown for the Orion Bar and the S140 PDR. However, the SiO/CS abundance ratio in the Orion Bar is 2 orders of magnitude lower than toward the SW CND and the 20 GMC. Thus, UV photo-desorption does not seem to play an important role in the enhancement of SiO in the central 12-pc of the GC.

On the other hand, the SiO/CS abundance ratio in IC443−G is very similar to those found toward the SW CND and the 20 GMC sources. However, the *plateau* component of Orion KL presents a SiO/CS abundance ratio that is one order of magnitude greater than those found at our sources. According to the C-shock models of Jiménez-Serra et al. (2008), our observed SiO abundances ($\sim 10^{-9}$) can be accounted for by the sputtering of grain mantles in shocks with velocities between 20 and 30 km s^{-1} (assuming that a significant amount of silicon is locked in the mantles). At higher shock velocities, sputtering

Table 6. Abundance ratios compared with prototypical Galactic and extragalactic sources.

Source		SiO/CS	$H^{13}CO^+$/CS	$HN^{13}C$/CS	HNCO/CS	$HN^{13}C/H^{13}CN$
SW CND		0.13	0.04	0.012	0.10	...
20 GMC		0.24	0.025	0.13	1.9	...
Galactic sources						
Orion Bar	(20″, −20″)	1.2×10^{-3}	2.0×10^{-3}	... / 6×10^{-4}	$\leq7\times10^{-4}$	... / 0.20
	(60″, −60″)	...	... / 0.015	... / 0.015	≤0.07	... / 1.9
IC443−G		0.3	≤0.03 / 0.015	... / 5×10^{-3}	...	... / 0.13
Orion KL−Plateau		2.0	...	...	0.6	...
Orion KL−Hot Core		0.05	...	...	0.3	...
TMC−1		$\leq1.5\times10^{-4}$	0.04	0.05	0.4	1.2
Extragalactic sources						
NGC 253		0.020	6×10^{-3}	4×10^{-3}	0.25	0.20
NGC 4945		≤0.03	0.025	0.08	1.0	1.6
M 82	Southwest	≤0.05	0.05	...	≤4	...
	Center	...	... / 9×10^{-3}	≤0.04 / 6×10^{-3}	≤1.2	... / 0.4
	Northeast	...	...	...	≤0.03	...
IC 342	Center	...	... / 0.010	... / 0.014	0.8	... / 0.4
	North	≤0.16	0.07	...	1.0	...
IC 342 (interf.)	A	(2.3–7)×10^{-3}	(1.7–5)×10^{-3}	... / (1.1–3)×10^{-3}	≤0.14	... / 0.23
	D	≥0.018	≥3×10^{-3}	... / ≥1.9×10^{-3}	≥0.25	... / 0.18
	D′	...	...	... / ≥1.8×10^{-3}	≥0.5	...

Notes.—When two values for the abundance ratio are presented, the first one has been derived from the ^{13}C isotopic species and the second one from the main isotope assuming $^{12}C/^{13}C\approx65$ for IC443−G and the Orion Bar (van Dishoeck et al. 1993; Jansen et al. 1995), and $^{12}C/^{13}C\simeq 40$ (Henkel et al. 1998) for the extragalactic sources. Interferometric column density ratios of IC 342 have been derived from $C^{34}S$ assuming a range of $^{32}S/^{34}S$ isotopic ratios of 8–23 (see Meier & Turner 2005).

of grain cores begins and gives rise to SiO abundances much higher ($\sim10^{-7}$–10^{-6}) than the ones derived toward the 12 central parsecs of the Galaxy.

Therefore, neither X-rays nor photo-desorption due to the UV field from the Central cluster can explain the SiO abundance in the central 12-pc sources, with C-shocks with velocities between 20–30 km s^{-1} the most likely origin of its abundance.

6.3. HNCO chemistry.

Isocyanic acid (HNCO) has been observed in a wide variety of sources, from dark clouds to hot cores (see the introduction of Tideswell et al. 2009 for a brief review) with abundances of $\sim10^{-9}$–10^{-8}. In the GC, HNCO emission has also been found to be particularly strong and widespread (Lindqvist et al. 1995; Kuan & Snyder 1996; Dahmen et al. 1997; Sato et al. 2002; Minh & Irvine 2006; Martín et al. 2008).

The HNCO/CS abundance ratio in the (20″, −20″) position of the Orion Bar is 2–3 orders of magnitude lower than in the central 12-pc sources. Moreover, among all the sources listed in Table 5, the Orion Bar is where one can find the lowest HNCO abundances. The behavior of HNCO in PDRs is completely opposite that of CS. Martín et al. (2008) have studied the HNCO emission toward several positions in the GC, finding that the HNCO abundance decreases by up to a factor 22 for the sources affected by photodissociation, with maximum values of 2×10^{-8} toward the cores of GMCs and minimum values of 1×10^{-9} toward the sources close to massive stellar clusters. Moreover, this difference factor increases up to 30 when the HNCO/CS abundance ratio is compared. The HNCO abundance toward the SW CND is one order of magnitude lower than toward the 20 GMC, which is consistent with the idea that HNCO is very easily photodissociated by UV radiation, as the SW CND is closer to the Central cluster and/or not as well-shielded as the 20 GMC.

Martín et al. (2009b) have modeled the HNCO abundance in PDRs as a function of the visual extinction with T_K= 50 K, n_{H_2}= 10^5 cm^{-3}, and a UV radiation field of G_0= 5×10^3 in Habing units, similar to the physical conditions of galactic nuclei. In their coupled dense core-PDR model, they find observable HNCO abundances only for $A_v \geq 5$ (i.e. $N_{H_2} \sim 5\times10^{21}$ cm^{-2}), concluding that molecular clouds affected by UV radiation with observable HNCO abundances must contain well shielded dense cores where HNCO molecules are protected against UV photons. According to Martín et al. (2009b), this could be the reason the HNCO/CS ratio show a wide range of values toward extragalactic nuclei, from the upper limit of 0.03 in M 82−NE to the high values (0.8–1.0) found toward IC 342 and NGC 4945, with the ratio in NGC 253 in between (0.25; see Table 6). The low ratio measured toward the GMCs of M 82 is the result of large amounts of gas being affected by UV radiation in its nuclear region. This is due to the lower column densities that M 82 GMCs present in comparison with GMCs of other extragalactic nuclei, where higher HNCO/CS ratios are found (Martín et al. 2009b).

Therefore, our low measured value for the HNCO/CS abundance ratio toward the SW CND reflects the effect of UV radiation on the fragile HNCO molecules. Column densities measured in the 12 central parsecs are $\sim10^{22}$ cm^{-2}, with the lowest values found toward Cloud A and the NE CND, just the sources where no emission of HNCO has been detected.

In contrast to the destruction mechanism of HNCO, the origin of this species is not yet well understood. Gas-phase chemistry alone is not able to reproduce the observed HNCO abundances, predicting abundances on the order of 10^{-10} (Iglesias 1977). Chemistry in post-shocked gas driven by neutral-neutral reactions has been invoked to reproduce HNCO abundances on the order of 10^{-8}, as the high temperatures achieved by shocks could overcome the energy

barriers of these reactions (for more details see Turner et al. 1999; Tideswell et al. 2009; Rodriguez-Fernandez et al. 2010). However, this formation pathway presents two main drawbacks: the short times that shocks can maintain the required high temperatures and cannot detect O_2 in the Sgr A complex ($X_{O_2} \leq 1.2\times10^{-7}$; Sandqvist et al. 2008), a key molecule in this formation path of HNCO.

The alternative to HNCO production in gas phase is formation through grain-surface chemistry. Hot core chemical models (Garrod et al. 2008; Tideswell et al. 2009), as well as gas-grain chemistry models in cold clouds (Hasegawa & Herbst 1993), generate high abundances of HNCO in the grain mantles (10^{-7}–10^{-5}). There are also observational clues that point to a grain-surface origin for HNCO: the "XCN" infrared (IR) absorption feature of interstellar ices that could correspond to the OCN^- anion (Hudson et al. 2001). Another observational proof is the correlation between the HNCO and SiO-integrated and peak intensities found by Zinchenko et al. (2000), with SiO lines broader than HNCO lines, which suggests a common origin. Besides, HNCO abundances are also enhanced in high-velocity gas (Zinchenko et al. 2000). Moreover, the largest SiO/CS and HNCO/CS abundance ratios among our selected prototypical Galactic sources are found at the *plateau* component of the Orion KL cloud, a high-mass star-forming region affected by several outflows.

However, after the formation of HNCO on the grain mantles, according to hot core chemical models, HNCO is destroyed by reactions with radicals originating more complex species, such as NH_2CHO. Under this scenario, the observed HNCO abundances in the gas-phase would be the result of the destruction of these more complex molecules (Garrod et al. 2008; Tideswell et al. 2009). Ejection of more complex molecules with the subsequent photodissociation and production of HNCO in gas-phase also seems unlikely in the GC sources, as we observed the highest HNCO abundances toward the more shielded cores of the GMCs and the lowest ones toward regions with strong UV fields that should favour the destruction of the complex molecules. Moreover, observational results seem to contradict the idea of HNCO as a *second generation* species. Bisschop et al. (2007) have measured a set of complex organic molecules toward a sample of hot cores. HNCO and NH_2CHO belong to the same group, that is, they are evaporated from grain mantles and are very likely *first generation* species (i.e. directly released from the grains), as their abundances toward several sources are correlated.

Therefore, HNCO could share the same origin as SiO, shocks, but HNCO seems to be more sensitive to UV radiation. IC 342, a similar nearby galaxy to the Milky Way, has been mapped with interferometry technique in several species, revealing an spiral galaxy composed of several GMCs with chemistries driven by different mechanisms. The SiO/CS and HNCO/CS ratios toward the GMC closer to the stellar cluster (GMC A) in IC 342 are lower than those found toward the GMCs in the spiral arms (GMCs D and D′). The same trend is followed by our SW CND and 20 GMC sources, with the upper limit to the HNCO/CS abundance ratio at the GMC A of IC 342 similar to our derived value at the SW CND source. The GMC A could be suffering the direct impact of the UV radiation, stellar winds, and SN explosions originated in the central cluster (Schinnerer et al. 2008). Therefore, both sources seem to be affected by strong UV radiation and shocks. In contrast, the GMCs in the spiral arms of IC 342 show higher lower limits to the SiO/CS and HNCO/CS ratios, which could approach the 20 GMC ratios. This is consistent with the idea that the GMCs in the spiral arms are affected by shocks, but not strongly by UV radiation. Meier & Turner (2005) also mapped methanol (CH_3OH), finding abundance enhancements that can be produced by large-scale mild shocks due to orbital dynamics, as CH_3OH cannot be ejected to the gas by evaporation and the emission of both species is widespread. Thus, interferometric observations of IC 342 seem to support the idea of grain chemistry as the origin of HNCO.

6.4. $H^{13}CO^+$ chemistry.

The $H^{13}CO^+$/CS abundance ratio toward the Orion PDR presents a difference of almost an order of magnitude between the offset positions (20″, −20″) and (60″, −60″) with respect to the ionization front (IF; see Table 6; Jansen et al. 1995) This difference is due to a larger increase in the CS abundance toward the closest position to the IF, which is (20″, −20″), whereas the HCO^+ abundance mostly remains constant. PDR-models show that higher HCO^+/CS abundance ratios are expected toward the superficial layers of PDRs than toward cool cores (Sternberg & Dalgarno 1995). The exception to this trend could be the most UV-exposed layer of PDRs. There, ion destruction is very efficient through dissociative recombination reactions, as electron densities reach their maximum values. In the Horsehead edge-on PDR, the HCO emission traces the edge of the PDR, whereas the $H^{13}CO^+$ emission appears more shifted to the cloud interior (Goicoechea et al. 2009).

Our $H^{13}CO^+$/CS abundance ratios are similar to that of the (60″, −60″) position of the Orion Bar, although the SW CND ratio is slightly larger (by factors of 2−2.6) and more similar to the value found at the dark cloud TMC-1, despite the strong UV field that impinges on the CND. This could be due to the different extension sampled by the telescope beam in the Jansen et al. survey (0.04 pc) and our work (1.2 pc). Our beam samples not only the PDR, but also a more shielded part of the cloud. Thus, the $H^{13}CO^+$/CS abundance ratio could reflect this mixture, approaching the value found in dark clouds.

Conversely to the HCO^+ chemistry in PDRs and dark clouds, there is no agreement with a possible HCO^+ enhancement in shocks. Studies of molecular outflows (Garden & Carlstrom 1992; Girart et al. 1999) have found enhancements of the HCO^+ abundance in shocked gas. HCO^+ abundance enhancement of one order of magnitude have been detected in the interface between high-velocity outflows and the surrounding quiescent gas in low-mass star-forming regions (Hogerheijde et al. 1998). This enrichment would be produced by the sputtering of CO and H_2O to gas phase from ice mantles, followed by photochemical processing by UV radiation, generating C^+ that would react with H_2O to enhance the HCO^+ abundance (Rawlings et al. 2000; Viti et al. 2002). However, there are also chemical models and observational results that report a decrease in the HCO^+ abundance in the postshock gas with respect to the preshock gas (see van Dishoeck et al. 1993; Garay et al. 1998 and references therein).

Our SW CND and 20 GMC sources present values of the $H^{13}CO^+$/CS abundance ratio in between those of TMC-1, clump G, and the (60″, −60″) position of the Orion Bar. The highest value of this ratio is the one of TMC-1, a prototype of quiescent cloud. This suggests that the ion abundance in our sources is not increased by shocks, despite the favorable conditions that this region presents, i.e., shocks plus UV radiation.

6.4.1. The GC ionization rate.

Oka et al. (2005) claim that the GC presents a higher ionization rate than anywhere else in the Galaxy ($\zeta = 2 - 7 \times 10^{-15} s^{-1}$). H_3^+ absorption lines toward selected stars reveal the presence of extensive hot and diffuse clouds with high-velocity dispersions in the inner 200 pc of the Galaxy. Oka et al. (2005) found broad absorptions due to $H_3^+(3,3)$ in the direction of the 50 km s^{-1} GMC, consistent with its velocity range. However, Geballe et al. (1989), from CO in absorption, prefer to establish the absorption origin at the inner edge of the CND.

Farquhar et al. (1994) have studied the effects of varying the cosmic-ray ionization rate in dark clouds. Their model predicts an increase in the HCO^+ abundance as ionization rate becomes higher. Our HCO^+ abundances, derived taking a $^{12}C/^{13}C$ isotopic ratio of 20–25 (Wilson 1999) into account, are between $\sim 10^{-9}$–10^{-8}. The maximum value corresponds to the SW CND that, according to Farquhar et al.'s model, could be explained by the "standard" cosmic-ray ionization rate ($\zeta \sim 10^{-17}$ s^{-1}). On the other hand, the minimum value, corresponding to the 50 GMC, could be produced by an ionization rate a factor of ~60 lower than the "standard" value. Therefore, a small gradient in the ionization rate could be responsible for the variations found in the $H^{13}CO^+$ abundances toward the CND and the 50 GMC. However, our values do not support the high ionization rate derived by Oka et al. (2005). When modeling of the observed intensities of H_2O and H_3O^+ toward the Sgr B2 envelope, van der Tak et al. (2006) obtain a cosmic-ray ionization rate of $\sim 4 \times 10^{-16}$ s^{-1}, lower than the value derived by Oka et al. (2005) in diffuse clouds. The physical conditions of the Sgr B2 envelope (T_k= 60 K and n_{H_2}= 10^6 cm^{-3}) are more similar to those of the molecular gas traced by our observations.

6.5. $HN^{13}C$ chemistry.

The chemistry of HNC is usually studied simultaneously with that of HCN. Unfortunately, we cannot compare $HN^{13}C$ with $H^{13}CN$ abundances in our sources. However, HCN and CS seem to share a constant abundance in regions dominated by different kinds of chemistries. Both species are not strongly affected by shocks or by UV radiation. Therefore, we expect that the $HN^{13}C$/CS and $HN^{13}C/H^{13}CN$ abundance ratios follow a similar trend. From Table 6, the lowest values of the $HN^{13}C/H^{13}CN$ abundance ratio are associated with the sources that present the lowest values of the $HN^{13}C$/CS abundance ratio, the (20″, −20″) position of the Orion Bar and IC443–G. Conversely, the highest values of both ratios are found toward the (60″, −60″) position of the Orion PDR and the dark cloud TMC-1. Following this trend, one can predict a lower $HN^{13}C/H^{13}CN$ abundance ratio at the SW CND compared with the 20 GMC. This result agrees with previous studies that suggest that the HNC molecule is very sensitive to temperature, since it is depleted toward regions of high temperatures caused by shock or UV-heating.

In quiescent cool dark clouds, the HNC/HCN abundance ratio is close to or higher than unity (2.1±1.2 in a range of 0.54–4.5; Hirota et al. 1998). The HNC/HCN ratio decreases by 1–2 orders of magnitudes in the warmer GMCs near sites of massive star formation. Values ranging between 0.013–0.2 have been derived toward selected positions in the GMC OMC-1, with the lowest ratios found in the immediate vicinity of the hot core Orion-KL (Schilke et al. 1992). These results suggest a correlation between the HNC/HCN abundance ratio and temperature. Moreover, Hirota et al. (1998) claimed that this decrease in the ratio is due to destruction processes of HNC rather than to formation processes of HCN, as the HCN abundances in OMC-1 are almost the same than in dark cloud cores, whereas the HNC abundances in OMC-1 are generally lower. According to gas-phase chemical models, HCN and HNC are mainly produced by dissociative recombination of $HCNH^+$, leading to HNC on 60% and HCN on 40% of collisions, as observed abundances toward cold dark clouds suggest (Hirota et al. 1998). The dependence of HNC abundance on temperature has been explained by Pineau des Forets et al. (1990) as due to neutral-neutral reactions with an activation barrier. Hirota et al. (1998) derived an activation barrier of 190 K for the destruction reactions of HNC with H and O. However, this value could be higher according to quantum chemical calculations, making the destruction of HNC effective only in regions with temperatures higher than 300 K (Talbi et al. 1996).

As we can see in Table 3, the 20 GMC is the source that presents the lowest volume density of all our sources, with n_{H_2}= 0.4×10^5 cm^{-3} at T_K= 50 K. As previously mentioned, a decrease in the temperature is compatible with an increase in the volume density. Thus, the 20 GMC could present a lower density or, alternatively, a lower temperature than the surrounding molecular gas, leading to less efficiency of the HNC destruction processes there.

6.6. The chemistry of the central 12 parsecs of the GC.

In summary, from the comparison of the abundance ratios derived toward the 12 central parsecs of the GC with that of prototypical Galactic sources, one can clearly conclude that shocks are responsible for maintaining the high SiO abundances found at the CND and the GMCs, while the strong UV radiation also affects the dense gas of the CND. This strong UV field seems to be responsible for the low abundances of HNCO and $HN^{13}C$ measured toward the CND. Increasing temperatures due to UV-heating as one approaches the Central cluster could be responsible for the observed decrease in the $HN^{13}C$ abundance. The $HN^{13}C$ peak abundance is found toward the well-shielded 20 GMC, a molecular cloud that could be either less dense or colder than the surrounding molecular gas. As shocks are widespread all over the central region, it is not expected that they have produced the differences found in the $HN^{13}C$ abundances. High temperatures can also favor HNCO formation in gas-phase. However, our observed abundance ratios toward the CND indicate that HNCO abundance is strongly depleted there, as well as in Galactic PDRs. The high SiO and HNCO abundance ratios found toward the 20 and 50 GMCs can be explained by the presence of nondissociative C-shocks with velocities between 20 and 30 km s^{-1}, able to eject Si or SiO from grain mantles into the gas phase. HNCO could also be locked in grain mantles and directly realeased to the gas phase by these C-shocks. Once in the gas phase, unshielded HNCO molecules would be rapidly destroyed by the UV radiation, leading to the low HNCO abundances found at the CND molecular gas. The small gradient found in the $H^{13}CO^+$ abundance from the CND to the 50 GMC could be explained by a decrease of one order of magnitude in the ionization rate with respect to the "standard" value toward this GMC, which presents the highest column density of all our sources.

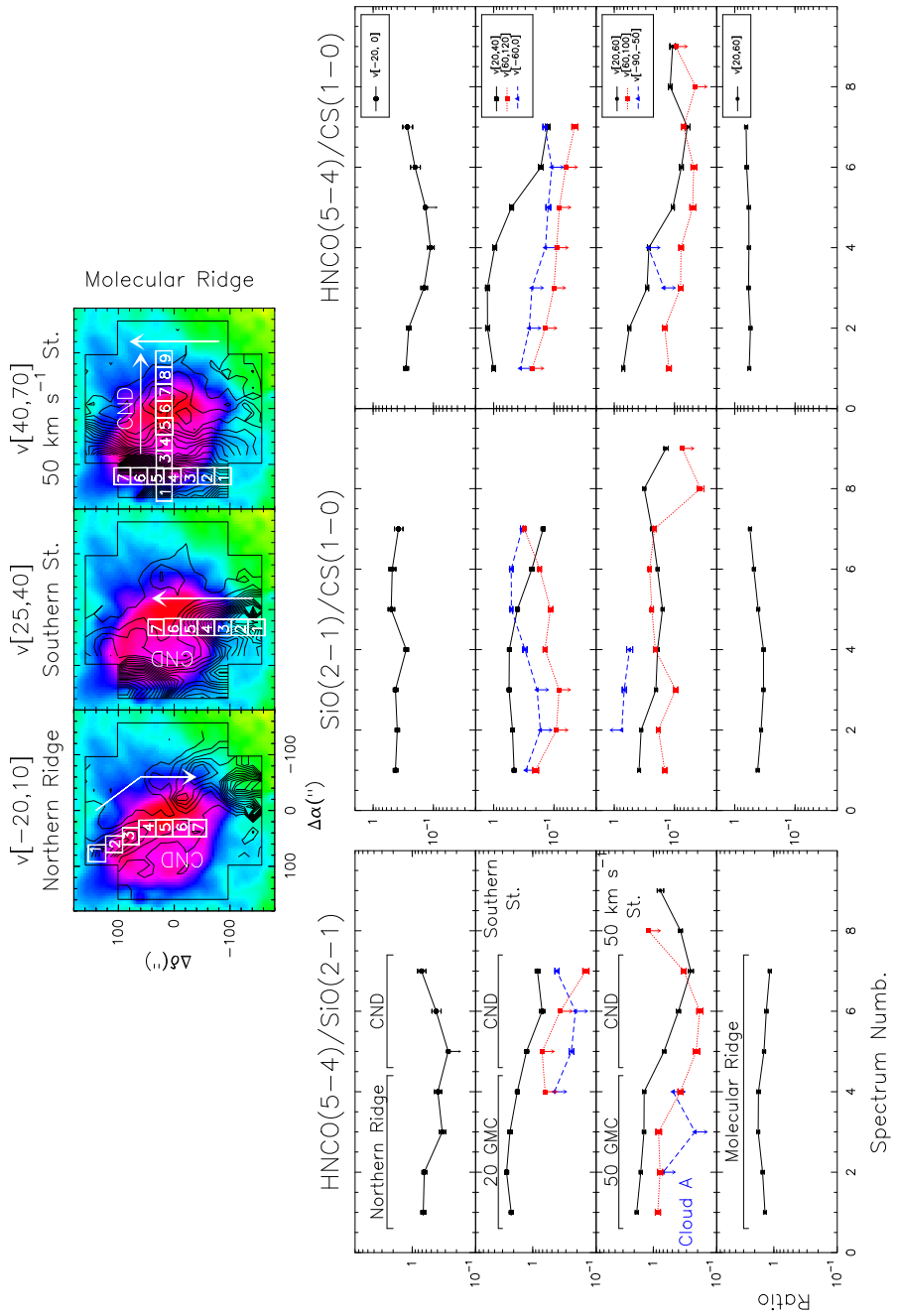

Fig. 10. Velocity-integrated HNCO(5–4)/SiO(2–1) (left), SiO(2–1)/CS(1–0) (middle), and HNCO(5–4)/CS(1–0) (right) ratios along four different directions and different velocity intervals. The four different directions are indicated at the top of the left panels, and they are pointed out with white arrows on the three maps located at the top of the figure. These maps show, in contours, the SiO(2–1) emission in three different velocity ranges (indicated at the top of each map), superimposed on the radio continuum image of Yusef-Zadeh & Morris (1987) at 20 cm on a color scale. The different velocity intervals in which we have integrated the molecular emission are indicated at the upper-right corner of the right panels. For example, three velocity-integrated ratios are shown along the Southern Streamer direction. The one corresponding to the velocity interval of this streamer, [20, 40] km s^{-1}, is shown with black circles connected by black lines, whereas those corresponding to lower and higher velocity intervals, [−60, 0] and [60, 120] km s^{-1}, are represented by blue triangles connected by dashed lines and red squares connected by dotted lines, respectively. The x-axis of the ratio plots represents the spectrum number, that increases from northeast to south in case of the Northern Ridge (1st plot beginning from the top), from south to north in the Southern Streamer (2nd), from east to west in the 50 km s^{-1} Streamer (3rd), and from south to north in the Molecular Ridge (4th), i.e., in the direction of the white arrows. The white open squares, marked with the spectrum numbers, surround the region where the ratios have been derived, whose spectra can be seen in Fig. 11. Uncertainties in the ratio values represented by the errorbars have been calculated propagating the uncertainties in the intensities, which have been derived assuming a conservative 20% calibration error.

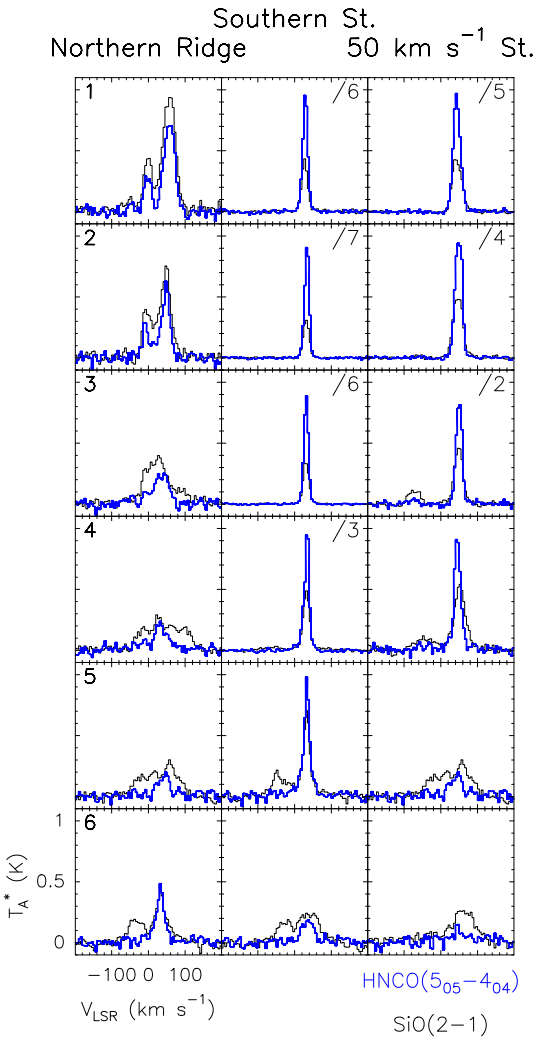

Fig. 11. SiO(2–1) (black line) and HNCO(5–4) (thick blue line) selected spectra taken along the Northern Ridge (left column), Southern Streamer (middle column) and 50 km s^{-1} Streamer (right column). In the maps at the top of Fig. 10, the areas where the spectra have been obtained can be seen as white open squares. Their numbers appear in the upper-left corner of each spectrum of the left column. The intensity of SiO(2–1) and HNCO(5–4) have been divided in some cases by a factor shown in the upper-right corner of the corresponding panel.

6.7. The HNCO(5–4)/SiO(2–1) ratio as a probe of the distance to the nuclear region.

The abundance ratios derived in Sect. 5 show a possible relation between the HNCO/SiO ratio and the distance to the nuclear region. The HN^{13}C/H^{13}CO$^+$ and HNCO/H^{13}CO$^+$ abundance ratios present a similar trend, with the most contrasted column density ratios. However, H^{13}CO$^+$ suffers from absorption in the direction of Sgr A*, whereas the HN^{13}C emission is not in general very intense. On the other hand, SiO and HNCO present strong emission in the regions where they are detected. As we have previously discussed in Sects. 6.2 and 6.3, SiO and HNCO seem to share a common origin, that is, both molecules are locked in grain mantles and can be released to the gas phase by shocks. However, HNCO is photodissociated more efficiently than SiO. In Sect. 5 we have also seen that excitation effects do not modify the general trends found in the integrated intensity ratio maps. Therefore, the HNCO/SiO intensity ratio should provide information on the relative distance of the observed molecular gas to the Central cluster, the source of the UV radiation giving rise to the photodissociation in the nuclear region (Krabbe et al. 1995; Figer 2008).

The HNCO(5–4) emission not only decreases in the high-velocity gas, but also in the velocity components related to the GMCs. Figure 10 shows the HNCO(5–4)/SiO(2–1), SiO(2–1)/CS(1–0), and HNCO(5–4)/CS(1–0) intensity ratios (hereafter the HNCO/SiO, SiO/CS, and HNCO/CS ratios) for low, intermediate, and high-velocity gas ranges along four different directions. The Northern Ridge (velocity range between [−20, 0] km s^{-1}), the Southern Streamer ([−60, 0], [20, 40], and [60, 120] km s^{-1}), the 50 km s^{-1} Streamer ([−90, −50], [20, 60], and [60, 100] km s^{-1}), and the Molecular Ridge ([20, 60] km s^{-1}). Maps at the top of Fig. 10 indicate the spatially integrated regions where we derived the integrated instensity ratios. In the following, we discuss each of this streamers comparing our instensity ratios with the previous pictures of the 3D arrangement proposed in the literature, trying to place them along the LOS:

–**The Molecular Ridge:** The intensity ratio along these ridge is a good example of a rather constant HNCO/SiO ratio with only differences of a factor of 1.5 between the maximum and minimum observed values. This suggests that there the molecular gas is not strongly affected by UV radiation due to its distance to the UV source and/or its shielding from the UV photons. The values of the HNCO/SiO, SiO/CS, and HNCO/CS ratios are around 1.8, 0.6, and 0.6, respectively.

–**The Northern Ridge:** This filamentary feature is located on the northern edge of Sgr A East, as can be seen from the [−20, 10] km s^{-1} map at the top-left of Fig. 10. This ridge shows low HNCO/SiO ratios (<0.7) along all its full length (even for the more distant pixels from the nucleus), with a systematic decrease (by factor of ≥2.5) as we approach the center. This decrease must be due to the photodissociation of HNCO, as the SiO/CS ratio shows a constant value along its length (∼0.4). The HNCO/CS ratio is low (0.11–0.3) compared to that of the Molecular Ridge and the GMCs. It is likely that an even larger change in the HNCO/SiO ratio could be achieved along this filament if the mapped area would have been extended further to the north of the ridge, as this feature seems to be connected with the −30 km s^{-1} molecular cloud (Serabyn & Güsten 1987). Our results support the idea that this cloud could be feeding the CND through the Northern Ridge.

McGary et al. (2001) find a connection between this ridge and the northeastern region of the CND. These authors find a smooth positive velocity gradient in their NH_3 maps from north to south (from −10 km s^{-1} in the Northern Ridge to 60 km s^{-1} in the as a function northeastern region of the CND). In the case that interaction between the ridge and the CND occurs, this velocity gradient places the ridge in front of the northeastern part of the CND. A similar gradient can be observed in the declination-velocity plot of the SiO(2–1) emission averaged between RA= [45″, 105″] in Fig. 3. McGary et al. (2001) also find an increase in the $NH_3(2,2)/NH_3(1,1)$ line ratios that suggests an increase in temperature where the streamer intersects the CND.

Dust emission is also observed from the ridge, but it disappears in the connexion region between the CND and the ridge, which McGary et al. (2001) interpret as destruction of dust by UV-photons from the Central cluster. However, Lee et al. (2008) suggest, from their kinematical comparison of shocked gas traced by H_2 emission with quiescent gas traced by NH_3 emission, that this feature is on the far side of the Sgr A East SNR,

and is accelerated away from us due to the SNR expansion. Both scenarios would be irreconcilable. In the case that the nuclear region were inside or in the leading edge of Sgr A East and the Northern Ridge were behind the SNR, the Northern Ridge could not be connected with the CND. Karlsson et al. (2003) have carried out an interferometric mapping of the Sgr A complex in the four 18–cm OH absorption lines. The Northern Ridge is clearly seen in their 1665 and 1667 MHz maps, providing a strong argument against the idea of Lee et al. (2008), suggesting that the ridge is in front of the Sgr A East SNR, i.e.: in front of the continuum emission. Our low HNCO/SiO ratio implies the Northern Ridge must be close to the nucleus, which supports the interaction scenario.

–**The Southern Streamer:** This long filament extends northward from the 20 km s^{-1} GMC toward the southeastern edge of the CND. It has been observed in several transitions of NH_3 (Okumura et al. 1991; Ho et al. 1991; Dent et al. 1993; Coil & Ho 1999, 2000; McGary et al. 2001; Herrnstein & Ho 2002, 2005), and in methanol (Szczepanski et al. 1991). The HNCO/SiO ratio along the Southern Streamer shows the largest gradient with a variation of a factor of ∼18 between the ratio in the GMC (∼2.6 in the intermediate-velocity range) and in the CND (∼0.15 in the high-velocity range). Furthermore, the HNCO/CS ratio decreases by a factor of 28, with extreme values of ∼1.3 and ∼0.05 in the GMC and the CND, respectively. This decrease in the ratio values as we move toward the center is also observed if we only consider the intermediate velocity range (a difference of a factor of 4 in the HNCO/SiO ratios), which could indicate that this streamer is approaching the central region and, therefore, a possible connection with the CND. Similar to the Northern Ridge, this decrease in the ratio is probably caused by the photodissociation of the HNCO, together with the enhancement of the SiO abundance in the CND, combined with a less effective photodissociation rate of HNCO in the GMC. The SiO/CS ratio decreases by a factor of 4 as we approach the center in the intermediate velocity range, whereas the HNCO/CS ratio decreases in a factor of 10. The SiO and HNCO line profiles for the 20 km s^{-1} GMC are very similar, peaking at the same velocities as one approaches the center. However, the high-velocity gas of the CND only appears in the SiO emission (see the middle column of Fig. 11).

No velocity gradient has been detected along the Southern Streamer (Ho et al. 1991); therefore, if gas is accelerated along it, it must occur mainly perpendicular to the LOS, which complicates the connection between the CND and the 20 km s^{-1} GMC, since the GMC is located in front of the nucleus (Güsten & Downes 1980; Park et al. 2004). Montero-Castaño et al. (2009) have compared the HCN(4–3)/HCN(1–0) intensity ratio map of the central region, which traces highly excited material in the CND, with the $NH_3(3,3)$ and (6,6) observations (Herrnstein & Ho 2005), which trace the Southern Streamer and very warm gas, respectively. They find that at the location where the northeast part of the Southern Streamer and the southeastern part of the CND meet, the strongest peak in the $NH_3(6,6)$ emission and a region of high HCN(4–3)/HCN(1–0) ratio are found. Therefore, they propose that the impact of the Southern Streamer with the CND caused the infall of material toward the black hole, which is responsible for the highly excited gas found as we approach the center. Additionally, Sato & Tsuboi (2008), from interferometric observations, find an increase in the SiO(2–1)/$H^{13}CO^+$(1–0) ratio at the possible interaction site between the southeastern region of the CND and the Southern Streamer, together with larger line widths. Another probe for shocks in this possible interaction site is the 36 GHz methanol maser recently found by Sjouwerman et al. (2010) (see their Fig. 2) with a velocity of 22 km s^{-1} (these Class I masers are collisionally pumped and considered as typical signposts of shock-excited material). Moreover, Lee et al. (2008) claim that the SNR Sgr A East drives shocks into the northernmost part of the Southern Streamer and the southern part of the CND, pushing the gas toward us. These interactions with the SNR make the connection between the Southern Streamer and the CND possible. Therefore, the decrease in the HNCO/SiO ratio as the Southern Streamer approaches the nuclear region confirms the interaction between the Southern Streamer and the CND.

–**The 50 km s^{-1} Streamer:** This ridge of gas extending westward from the 50 km s^{-1} GMC was first detected by Szczepanski et al. (1991) in methanol and was also observed in HCN(3–2) by Marshall et al. (1995). This streamer could be a possible connection between the 50 km s^{-1} GMC and the northern lobe of the CND. Our data show a decrease in the HNCO/SiO ratio that would indicate that this streamer is approaching the nucleus; however, if we compare the SiO(2–1) and HNCO(5–4) spectra extracted from the possible interaction region between the streamer and the CND (spectrum number 4 in the right column in Fig. 11), it seems that both molecules are tracing different gas components. The HNCO(5–4) line is tracing the 50 km s^{-1} GMC with very similar profiles to spectra with numbers <4, which sample the inner region of this molecular cloud. All of these HNCO profiles do not show line widths that are too broad, ∼(19–23) km s^{-1}. In contrast, the SiO(2–1) lines taken at the same positions show an increase in the line widths from ∼(27–31) km s^{-1} (spectra with numbers <4) to 37 km s^{-1} (spectrum number 4). Moreover, the central velocity of the SiO(2–1) line is slightly redshifted with respect to the HNCO(5–4) line in spectrum number 4.

Marshall et al. (1995) do not detect any velocity gradient along the feature, and considering that the GMC is located behind the SNR Sgr A East, the connection is unlikely unless part of this GMC lies in the same plane as the northern lobe of the CND. In that case, the gas would run perpendicular to the LOS and no velocity gradient would be expected (Marshall et al. 1995). They suggest that this apparent connection could also be due to the overlapping of material from the GMC and the CND, as their HCN(4–3) maps suggest. Therefore, in this case, the decrease in the HNCO/SiO ratio could be produced by the blending of two gas components and not to a real interaction: the 50 km s^{-1} GMC, where the HNCO is more prominent than the SiO line, and gas from the CND, where the HNCO line disappears because of photodissociation from the central UV radiation and SiO emission is broadened by shocks.

There are two other features, Cloud A and the Western Streamer, that do not seem to be connected with the CND, but their low HNCO/SiO ratio indicates that they are close to the nuclear region. Both features seem to be related to the SNR Sgr A East:

–**Cloud A:** This cloud was previously observed by Genzel et al. (1990) in $C^{18}O$(2–1), and mapped by Sutton et al. (1990) in CO(3-2) and Serabyn et al. (1992) in CS(5–4) and CS(7–6). In addition, Serabyn et al. (1992) found a redshifted emission (80–85 km s^{-1}) just to the south of Cloud A. Both high-velocity emission components lie just inside of the compressed ridge of the 50 km s^{-1} GMC, which suggests that the molecular gas of this GMC had been accelerated to very high velocities by the expansion of Sgr A East. The accelerated

molecular gas appears on the front and the back sides of the expanding radio shell. Wright et al. (2001) support this scenario from their interferometric HCO^+ and HCN maps, together with other near blue and redshifted clumps of gas inside of the compressed ridge. A different interpretation was proposed by Liszt & Burton (1995), who detected this feature with very strong emission in CO(3–2) at v≤ −40 km s^{-1}, but they considered this feature as an extension of the high-longitude forbidden-velocity part of the CND, as they see a connection between it and the emission arising from the southwestern region of the CND, concluding that Cloud A was not an isolated feature.

From the declination-velocity cut made through it (panel RA=[45″, 105″] in Fig. 8), this cloud does not appear to be kinematically connected to either the 50 km s^{-1} GMC or to any other gas component. The SiO/CS and HNCO/SiO ratios in this cloud (∼ 0.7 and ≤ 0.22, respectively; see Fig. 10) suggest there are shocks, as well as UV-radiation, which also explain the lack of NH_3 and 1.2 mm dust emission, since the ammonia molecules and dust grains are destroyed by photodissociation and shocks, respectively (see Fig. 9 of McGary et al. 2001). Shocks could be caused by the expansion of Sgr A East SNR into this cloud, whereas UV-radiation could originat in the Central cluster, locating this cloud close to the nuclear region. The SiO/CS ratio in Cloud A is one of the highest found in the region, only exceeded by the southwest lobe of the CND. This fact could be explained by the geometry of the shock, that could be almost along the LOS. Additional support for the SNR interaction scenario comes from the central velocities of the SiO(2–1) and CS(1–0) profiles. The SiO(2–1) central velocity is offset by −11±3 km s^{-1} with respect to that of CS(1–0), indicating that Cloud A is pushed toward us by the SNR Sgr A East, if we consider that SiO traces more efficiently the shocked gas, whereas CS traces more quiescent gas. Moreover, Cloud A is detected in the 18–cm OH absorption maps of Karlsson et al. (2003) (in the 1665 and 1667 MHz lines), which locates it in front of the continuum emission of the SNR, consistent with our finding

-The Western Streamer: This feature is a long curved filamentary structure that closely matches the western edge of Sgr A East. McGary et al. (2001) reports a velocity gradient of 1 km s^{-1} arcsec^{-1} along its 150″ length. The southern half has a negative velocity whereas the northern half has a positive velocity, consistent with a ridge of gas highly inclined to the LOS that is pushed outward by the expansion of the SNR. The northern part of the streamer would be located on the far side of the SNR producing the redshifted emission, whereas the southern part would be located on the front side of the shell producing the blueshifted velocities (McGary et al. 2001; Lee et al. 2008). The SiO/CS ratios in this streamer present intermediate values of 0.3−0.4. On the other hand, the HNCO/SiO ratios seem to be low (0.3−0.4) with very low-intensity emission of HNCO, just slightly over the rms noise. This enhancement in the SiO/CS ratios could be attributed to shocks caused by the expansion of the SNR Sgr A East into the molecular filament. The smaller enhancement of the ratio with respect to the enhancement observed in the southwestern lobe of the CND and Cloud A could be due to the geometry of the interaction. In this case it must be highly inclined and orthogonal to the LOS. The Western Streamer is not detected in the 1.2 mm dust emission map (see Fig. 9 of McGary et al. 2001). These authors propose that the gas of the streamer could originate closer to the nucleus, where most of the dust is destroyed by UV-photons from the central cluster, and then pushed outwards by the SNR. Our data suggest that the dust destruction is very likely caused by shocks. Molecular gas of the Western Streamer also presents the highest kinetic temperatures in the central 10 pc, even showing NH_3(6,6) emission that traces gas at ≥100 K (Herrnstein & Ho 2005).

In summary, the HNCO/SiO intensity ratio seems to be an excellent tool for locating the different gas components relative to the nucleus. While the 50 km s^{-1} Streamer seems to be due to the overlapping of two different gas components (CND + 50 km s^{-1} GMC gas), the Southern Streamer seems to be feeding the CND from the 20 km s^{-1} GMC, whereas the Northern Ridge remains a good candidate to also feed the CND, possible connecting the −30 km s^{-1} molecular cloud with the central region. The Western Streamer and Cloud A seem to be associated with the expansion of the SNR Sgr A East and located close to the nuclear region. This streamer would arise from the western border of the SNR interacting with the molecular gas, whereas Cloud A could be part of the 50 km s^{-1} GMC that has been pushed by the SNR toward us almost along the LOS.

7. Conclusions

We have presented maps of the central 12 pc of the GC in the $J = 2 \rightarrow 1$ transition of SiO, the $J = 5_{0,5} \rightarrow 4_{0,4}$ transition of HNCO, and the $J = 1 \rightarrow 0$ transition of $H^{13}CO^+$, $HN^{13}C$, and $C^{18}O$, observed with the IRAM-30m telescope at Pico Veleta, with an angular resolution of 30″.

The main results obtained from this work can be summarized as follow:

- The SiO(2–1) emission, observed in a velocity range of [−125, 130] km s^{-1}, perfectly traces the CND, as well as all the features previously identified in other high-density molecular tracers. The $H^{13}CO^+$(1–0) emission covers the same velocity range and follows the SiO morphology, except for the absorption features toward the radio continuum source Sgr A*.
- In contrast, the HNCO(5–4) molecular line shows emission in the narrowest velocity range ([−30, 85] km s^{-1}). This molecular line presents the strongest emission of all the observed lines; however, its emission is concentrated in the GMCs and the Molecular Ridge, quickly disappearing as one approaches the Central cluster. Similar behavior is shown by the $HN^{13}C$(1–0) emission.
- The $C^{18}O$(1–0) emission is affected by contamination with foreground gas due to its lower critical density.
- Emission mostly coming from $NH_2CHO(5_{1,4}-4_{1,3})$ has been detected toward the GMCs and the Molecular Ridge.
- Using the LVG approximation, volume densities of $\sim 10^5$ cm^{-3} assuming T_K= 50 K are derived for all the gas components, expect for the the 20 km s^{-1} GMC, which could be either less dense or colder. In general, the highest densities are found toward the CND and Western Streamer, and the lowest ones toward the two GMCs.
- Hydrogen column densities have been derived from the high-density tracer CS, obtaining values of $0.5 - 6 \times 10^{22}$cm^{-2}, with the highest value found toward the 50 km s^{-1} GMC.
- The HNCO molecule shows the strongest contrast in column density and fractional abundance, with factors of ≥60 (≤ $0.8 - 50 \times 10^{13}$cm^{-2}) and 28 (∼ $0.7 - 19 \times 10^{-9}$), respectively. The highest values are found toward the cores of the

GMCs, whereas the lowest ones are derived toward the positions associated with the CND. A similar behavior is also found for $HN^{13}C$, with abundances $\sim 0.06 - 1.3 \times 10^{-9}$.

– SiO abundances do not follow the HNCO trend ($0.20 - 2.4 \times 10^{-9}$), with high values at the cores of the GMCs, as well as toward the CND, whereas $H^{13}CO^+$ shows the smallest variation in its fractional abundance ($0.05 - 0.4 \times 10^{-9}$). Thus, the observed species can be grouped into those whose abundances decrease (HNCO and $HN^{13}C$), and those whose abundances remain similar or are enhanced toward the nuclear region (SiO and $H^{13}CO^+$).
– From the comparison of the abundances derived toward the 12 central parsecs of our Galaxy with those of prototypical Galactic sources, one can conclude that non-dissociative C-shocks with velocities between 20–30 km s^{-1}, able to eject Si/SiO from the grain mantles to the gas phase, are responsible for maintaining the high SiO abundances found in the CND and the GMCs. HNCO could also be locked in grain mantles and directly realeased to the gas phase by the C-shocks. However, once in the gas phase, HNCO molecules are not well-shielded from the UV radiation coming from the Central cluster and would be rapidly destroyed, leading to the low abundances found in the CND. This strong UV field also seems to be responsible for the low abundances of $HN^{13}C$ measured toward the CND, as high temperatures could favor neutral-neutral reactions leading to the destruction of HNC molecules. The small gradient found in the $H^{13}CO^+$ abundance from the CND to the 50 km s^{-1} GMC could be explained by a decrease of one order of magnitude in the ionization rate with respect to the "standard" value toward the 50 km s^{-1} GMC.
– Ratios between SiO (which traces shocked gas), HNCO (shocked and/or photodissociated gas), and CS (quiescent dense gas) emissions provide an excellent tool for studing the possible connections and the 3D arrangement of the different features found in the central region of the Galaxy. From their comparison, we conclude that not only is the CND affected by UV radiation, but also the Western Streamer and Cloud A. The Southern Streamer and the Northern Ridge could be feeding the CND; however, the 50 km s^{-1} Streamer, composed of two overlapping components, does not seem to be connected with the CND.

Acknowledgements. The authors would like to thank Prof. M. Tsuboi and D. M. Montero-Castaño for kindly providing their CS(1–0) and HCN(4–3) data, respectively. We also thank the referee for the suggestions. This work was supported by the Spanish Ministerio de Ciencia e Innovación under project ESP2007-65812-C02-01.

References

Amo-Baladrón, M. A., Martín-Pintado, J., Morris, M. R., Muno, M. P., & Rodríguez-Fernández, N. J. 2009, ApJ, 694, 943
Bayet, E., Aladro, R., Martín, S., Viti, S., & Martín-Pintado, J. 2009, ApJ, 707, 126
Becklin, E. E., Gatley, I., & Werner, M. W. 1982, ApJ, 258, 135
Bisschop, S. E., Jørgensen, J. K., van Dishoeck, E. F., & de Wachter, E. B. M. 2007, A&A, 465, 913
Bradford, C. M., Stacey, G. J., Nikola, T., et al. 2005, ApJ, 623, 866
Burton, M. G., Hollenbach, D. J., & Tielens, A. G. G. M. 1990, ApJ, 365, 620
Christopher, M. H., Scoville, N. Z., Stolovy, S. R., & Yun, M. S. 2005, ApJ, 622, 346
Coil, A. L. & Ho, P. T. P. 1999, ApJ, 513, 752
Coil, A. L. & Ho, P. T. P. 2000, ApJ, 533, 245
Cummins, S. E., Linke, R. A., & Thaddeus, P. 1986, ApJS, 60, 819
Dahmen, G., Hüttemeister, S., Wilson, T. L., et al. 1997, A&AS, 126, 197
Davidson, J. A., Werner, M. W., Wu, X., et al. 1992, ApJ, 387, 189
Dent, W. R. F., Matthews, H. E., Wade, R., & Duncan, W. D. 1993, ApJ, 410, 650
Downes, D., Radford, S. J. E., Guilloteau, S., et al. 1992, A&A, 262, 424
Farquhar, P. R. A., Millar, T. J., & Herbst, E. 1994, MNRAS, 269, 641
Figer, D. F. 2008, ArXiv e-prints
Garay, G., Köhnenkamp, I., Bourke, T. L., Rodríguez, L. F., & Lehtinen, K. K. 1998, ApJ, 509, 768
Garden, R. P. & Carlstrom, J. E. 1992, ApJ, 392, 602
Garrod, R. T., Weaver, S. L. W., & Herbst, E. 2008, ApJ, 682, 283
Gatley, I., Jones, T. J., Hyland, A. R., et al. 1986, MNRAS, 222, 299
Geballe, T. R., Baas, F., & Wade, R. 1989, A&A, 208, 255
Genzel, R., Crawford, M. K., Townes, C. H., & Watson, D. M. 1985, ApJ, 297, 766
Genzel, R., Stacey, G. J., Harris, A. I., et al. 1990, ApJ, 356, 160
Ghez, A. M., Salim, S., Hornstein, S. D., et al. 2005, ApJ, 620, 744
Girart, J. M., Ho, P. T. P., Rudolph, A. L., et al. 1999, ApJ, 522, 921
Goicoechea, J. R., Pety, J., Gerin, M., Hily-Blant, P., & Le Bourlot, J. 2009, A&A, 498, 771
Goicoechea, J. R., Pety, J., Gerin, M., et al. 2006, A&A, 456, 565
Güsten, R. & Downes, D. 1980, A&A, 87, 6
Güsten, R., Genzel, R., Wright, M. C. H., et al. 1987, ApJ, 318, 124
Güsten, R. & Henkel, C. 1983, A&A, 125, 136
Güsten, R., Walmsley, C. M., & Pauls, T. 1981, A&A, 103, 197
Harris, A. I., Jaffe, D. T., Silber, M., & Genzel, R. 1985, ApJ, 294, L93
Hasegawa, T. I. & Herbst, E. 1993, MNRAS, 263, 589
Henkel, C., Chin, Y., Mauersberger, R., & Whiteoak, J. B. 1998, A&A, 329, 443
Herrnstein, R. M. & Ho, P. T. P. 2002, ApJ, 579, L83
Herrnstein, R. M. & Ho, P. T. P. 2005, ApJ, 620, 287
Hirota, T., Yamamoto, S., Mikami, H., & Ohishi, M. 1998, ApJ, 503, 717
Ho, P. T. P., Ho, L. C., Szczepanski, J. C., Jackson, J. M., & Armstrong, J. T. 1991, Nature, 350, 309
Hogerheijde, M. R., Jansen, D. J., & van Dishoeck, E. F. 1995, A&A, 294, 792
Hogerheijde, M. R., van Dishoeck, E. F., Blake, G. A., & van Langevelde, H. J. 1998, ApJ, 502, 315
Hudson, R. L., Moore, M. H., & Gerakines, P. A. 2001, ApJ, 550, 1140
Hüttemeister, S., Dahmen, G., Mauersberger, R., et al. 1998, A&A, 334, 646
Hüttemeister, S., Wilson, T. L., Bania, T. M., & Martin-Pintado, J. 1993, A&A, 280, 255
Iglesias, E. 1977, ApJ, 218, 697
Irvine, W. M., Goldsmith, P. F., & Hjalmarson, A. 1987, in Astrophysics and Space Science Library, Vol. 134, Interstellar Processes, ed. D. J. Hollenbach & H. A. Thronson Jr., 561–609
Jackson, J. M., Armstrong, J. T., & Barrett, A. H. 1984, ApJ, 280, 608
Jackson, J. M., Geis, N., Genzel, R., et al. 1993, ApJ, 402, 173
Jansen, D. J., Spaans, M., Hogerheijde, M. R., & van Dishoeck, E. F. 1995, A&A, 303, 541
Jiménez-Serra, I., Caselli, P., Martín-Pintado, J., & Hartquist, T. W. 2008, A&A, 482, 549
Jiménez-Serra, I., Martín-Pintado, J., Rodríguez-Franco, A., & Martín, S. 2005, ApJ, 627, L121
Karlsson, R., Sjouwerman, L. O., Sandqvist, A., & Whiteoak, J. B. 2003, A&A, 403, 1011
Krabbe, A., Genzel, R., Eckart, A., et al. 1995, ApJ, 447
Kuan, Y. & Snyder, L. E. 1996, ApJ, 470, 981
Lee, S., Pak, S., Choi, M., et al. 2008, ApJ, 674, 247
Lindqvist, M., Sandqvist, A., Winnberg, A., Johansson, L. E. B., & Nyman, L.-A. 1995, A&AS, 113, 257
Liszt, H. S. & Burton, W. B. 1995, ApJS, 98, 679
Liszt, H. S., Burton, W. B., & van der Hulst, J. M. 1985, A&A, 142, 237
Lo, K. Y. & Claussen, M. J. 1983, Nature, 306, 647
Lugten, J. B., Genzel, R., Crawford, M. K., & Townes, C. H. 1986, ApJ, 306, 691
Maeda, Y., Baganoff, F. K., Feigelson, E. D., et al. 2002, ApJ, 570, 671
Marcelino, N. 2007, PhD thesis, Universidad de Granada
Marcelino, N., Cernicharo, J., Tercero, B., & Roueff, E. 2009, ApJ, 690, L27
Marr, J. M., Wright, M. C. H., & Backer, D. C. 1993, ApJ, 411, 667
Marshall, J., Lasenby, A. N., & Harris, A. I. 1995, MNRAS, 277, 594
Martín, S., Martín-Pintado, J., & Mauersberger, R. 2009a, ApJ, 694, 610
Martín, S., Martín-Pintado, J., & Viti, S. 2009b, ApJ, 706, 1323
Martín, S., Mauersberger, R., Martín-Pintado, J., Henkel, C., & García-Burillo, S. 2006, ApJS, 164, 450
Martín, S., Requena-Torres, M. A., Martín-Pintado, J., & Mauersberger, R. 2008, ApJ, 678, 245
Martín-Pintado, J., Bachiller, R., & Fuente, A. 1992, A&A, 254, 315
Martín-Pintado, J., de Vicente, P., Fuente, A., & Planesas, P. 1997, ApJ, 482
Martín-Pintado, J., de Vicente, P., Rodríguez-Fernández, N. J., Fuente, A., & Planesas, P. 2000, A&A, 356, L5
McGary, R. S., Coil, A. L., & Ho, P. T. P. 2001, ApJ, 559, 326

Meier, D. S. & Turner, J. L. 2005, ApJ, 618, 259
Mezger, P. G., Zylka, R., Salter, C. J., et al. 1989, A&A, 209, 337
Minh, Y. C. & Irvine, W. M. 2006, New Astronomy, 11, 594
Montero-Castaño, M., Herrnstein, R. M., & Ho, P. T. P. 2009, ApJ, 695, 1477
Nummelin, A., Bergman, P., Hjalmarson, Å., et al. 2000, ApJS, 128, 213
Oka, T., Geballe, T. R., Goto, M., Usuda, T., & McCall, B. J. 2005, ApJ, 632, 882
Okumura, S. K., Ishiguro, M., Fomalont, E. B., et al. 1991, ApJ, 378, 127
Park, S., Muno, M. P., Baganoff, F. K., et al. 2004, ApJ, 603, 548
Pedlar, A., Anantharamaiah, K. R., Ekers, R. D., et al. 1989, ApJ, 342, 769
Persson, C. M., Olofsson, A. O. H., Koning, N., et al. 2007, A&A, 476, 807
Pineau des Forets, G., Roueff, E., & Flower, D. R. 1990, MNRAS, 244, 668
Rawlings, J. M. C., Taylor, S. D., & Williams, D. A. 2000, MNRAS, 313, 461
Reid, M. J. 1993, ARA&A, 31, 345
Requena-Torres, M. A., Martín-Pintado, J., Rodríguez-Franco, A., et al. 2006, A&A, 455, 971
Roberts, D. A. & Goss, W. M. 1993, ApJS, 86, 133
Rodriguez-Fernandez, N., Tafalla, M., Gueth, F., & Bachiller, R. 2010, ArXiv e-prints
Rodríguez-Fernández, N. J., Martín-Pintado, J., Fuente, A., et al. 2001, A&A, 365, 174
Sanders, R. H. 1998, MNRAS, 294, 35
Sandqvist, A., Larsson, B., Hjalmarson, Å., et al. 2008, A&A, 482, 849
Sato, F., Hasegawa, T., Dobashi, K., Kandori, R., & Whiteoak, J. B. 2002, in 8th Asian-Pacific Regional Meeting, Volume II, ed. S. Ikeuchi, J. Hearnshaw, & T. Hanawa, 205–206
Sato, M. T. & Tsuboi, M. 2008, Journal of Physics Conference Series, 131, 012033
Schilke, P., Pineau des Forêts, G., Walmsley, C. M., & Martín-Pintado, J. 2001, A&A, 372, 291
Schilke, P., Walmsley, C. M., Pineau Des Forets, G., et al. 1992, A&A, 256, 595
Schinnerer, E., Böker, T., Meier, D. S., & Calzetti, D. 2008, ApJ, 684, L21
Serabyn, E. & Güsten, R. 1987, A&A, 184, 133
Serabyn, E., Güsten, R., Walmsley, J. E., Wink, J. E., & Zylka, R. 1986, A&A, 169, 85
Serabyn, E., Keene, J., Lis, D. C., & Phillips, T. G. 1994, ApJ, 424, L95
Serabyn, E. & Lacy, J. H. 1985, ApJ, 293, 445
Serabyn, E., Lacy, J. H., & Achtermann, J. M. 1992, ApJ, 395, 166
Shukla, H., Yun, M. S., & Scoville, N. Z. 2004, ApJ, 616, 231
Sjouwerman, L. O. & Pihlström, Y. M. 2008, ApJ, 681, 1287
Sjouwerman, L. O., Pihlström, Y. M., & Fish, V. L. 2010, ApJ, 710, L111
Sternberg, A. & Dalgarno, A. 1995, ApJS, 99, 565
Sutton, E. C., Danchi, W. C., Jaminet, P. A., & Masson, C. R. 1990, ApJ, 348, 503
Szczepanski, J. C., Ho, P. T. P., & Gusten, R. 1991, in Astronomical Society of the Pacific Conference Series, Vol. 16, Atoms, Ions and Molecules: New Results in Spectral Line Astrophysics, ed. A. D. Haschick & P. T. P. Ho
Talbi, D., Ellinger, Y., & Herbst, E. 1996, A&A, 314, 688
Telesco, C. M., Davidson, J. A., & Werner, M. W. 1996, ApJ, 456, 541
Tercero, B., Cernicharo, J., Pardo, J. R., & Goicoechea, J. R. 2010, A&A, 517, A96+
Tideswell, D. M., Fuller, G. A., Millar, T. J., & Markwick, A. J. 2009, ArXiv e-prints
Tsuboi, M., Handa, T., & Ukita, N. 1999, ApJS, 120, 1
Turner, B. E., Terzieva, R., & Herbst, E. 1999, ApJ, 518, 699
Usero, A., García-Burillo, S., Martín-Pintado, J., Fuente, A., & Neri, R. 2006, A&A, 448, 457
van der Tak, F. F. S., Belloche, A., Schilke, P., et al. 2006, A&A, 454, L99
van der Tak, F. F. S., Black, J. H., Schöier, F. L., Jansen, D. J., & van Dishoeck, E. F. 2007, A&A, 468, 627
van Dishoeck, E. F., Jansen, D. J., & Phillips, T. G. 1993, A&A, 279, 541
Viti, S., Natarajan, S., & Williams, D. A. 2002, MNRAS, 336, 797
Vollmer, B. & Duschl, W. J. 2002, A&A, 388, 128
Wang, M., Henkel, C., Chin, Y., et al. 2004, A&A, 422, 883
Wilson, T. L. 1999, Reports on Progress in Physics, 62, 143
Wright, M. C. H., Coil, A. L., McGary, R. S., Ho, P. T. P., & Harris, A. I. 2001, ApJ, 551, 254
Yusef-Zadeh, F. & Morris, M. 1987, ApJ, 320, 545
Yusef-Zadeh, F., Stolovy, S. R., Burton, M., Wardle, M., & Ashley, M. C. B. 2001, ApJ, 560, 749
Zinchenko, I., Henkel, C., & Mao, R. Q. 2000, A&A, 361, 1079
Zylka, R., Mezger, P. G., & Wink, J. E. 1990, A&A, 234, 133

Appendix A: Velocity channel maps

Appendix B: Integrated intensity ratio maps

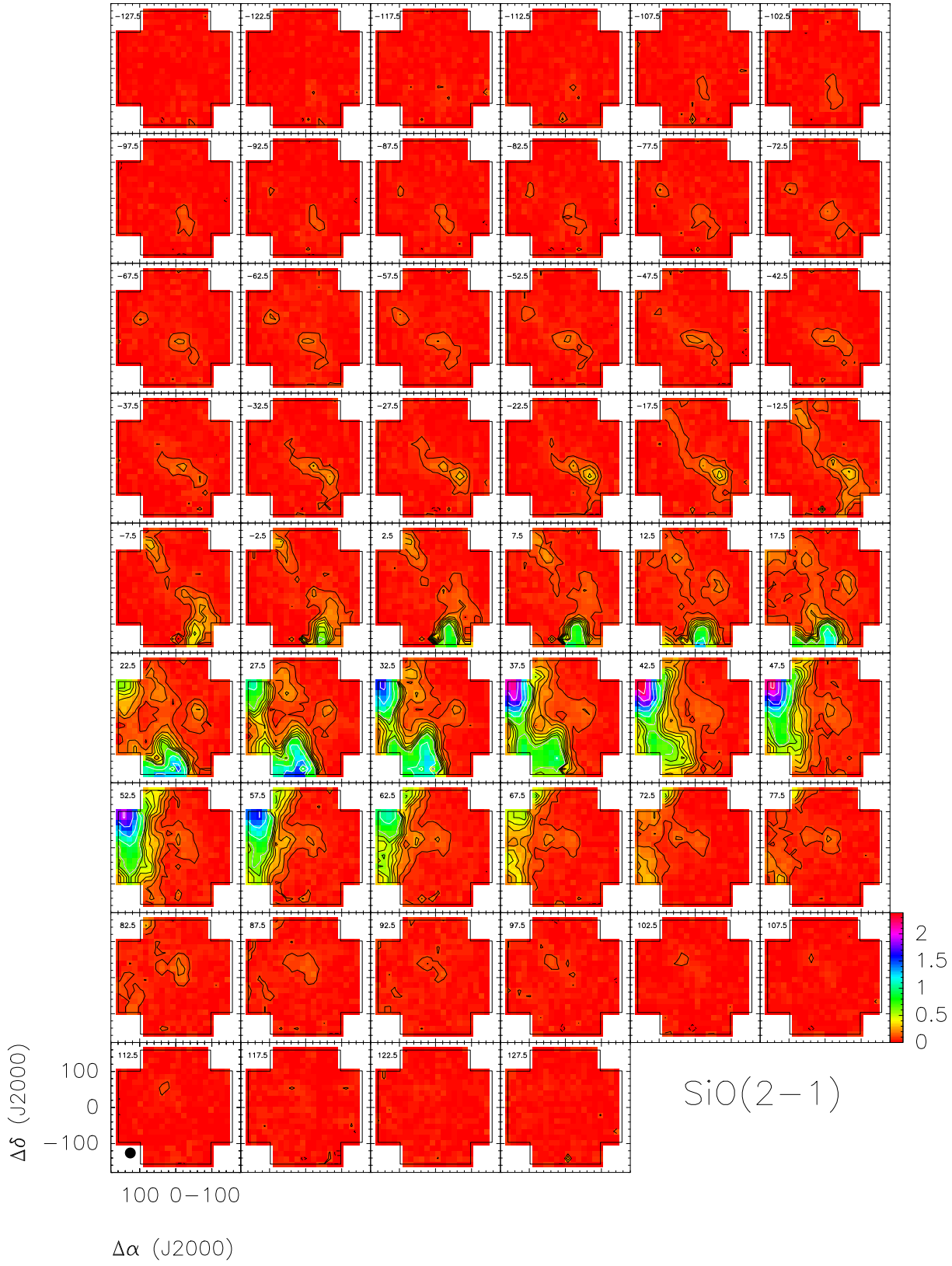

Fig. A.1. Velocity-channel maps of the SiO(2–1) emission. Black contour levels for the molecular line emission (in the T_A^* scale) are from 0.08 K (3σ) to 0.64 K in steps of 0.08 K. White contour levels are from 0.64 K in steps of 0.32 K. Dashed countours correspond to the -3σ level. Velocity channels range from −130 to 130 km s^{-1} by steps of 5 km s^{-1} (the velocity width per channel). The central velocities of the velocity-channel maps are shown in the upper-left corner of each panel. The wedge at the side shows the intensity scale of the SiO(2–1) emission. The beam size (30″) is shown at the bottom-left corner. Sgr A* is the origin for the offset coordinates (in arcseconds).

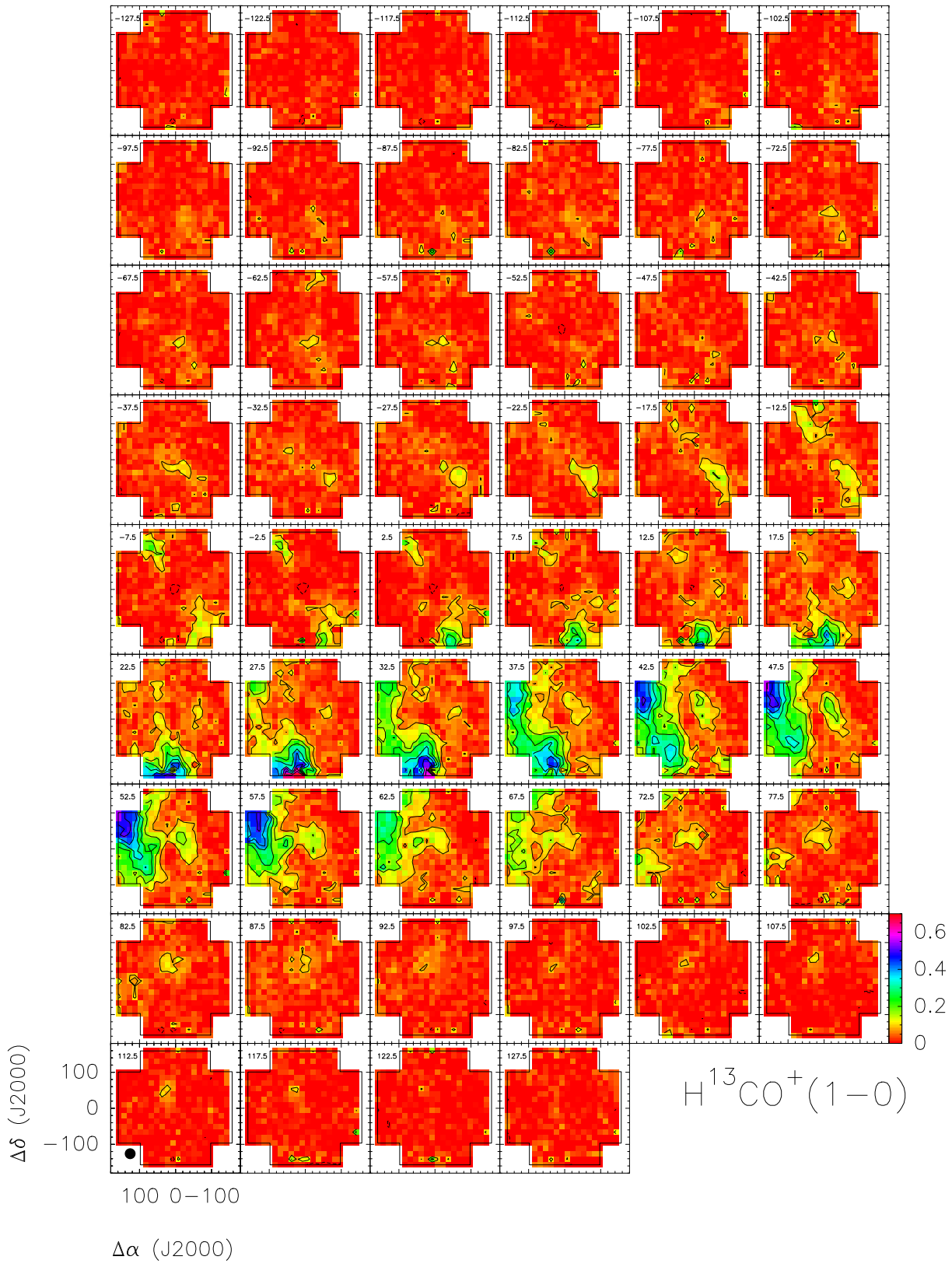

Fig. A.2. Velocity-channel maps of the $H^{13}CO^+$(1–0) emission. Contour levels for the molecular line emission are from 0.08 K (3σ) in steps of 0.08 K. The other characteristics of the figure are the same as in Fig. A.1.

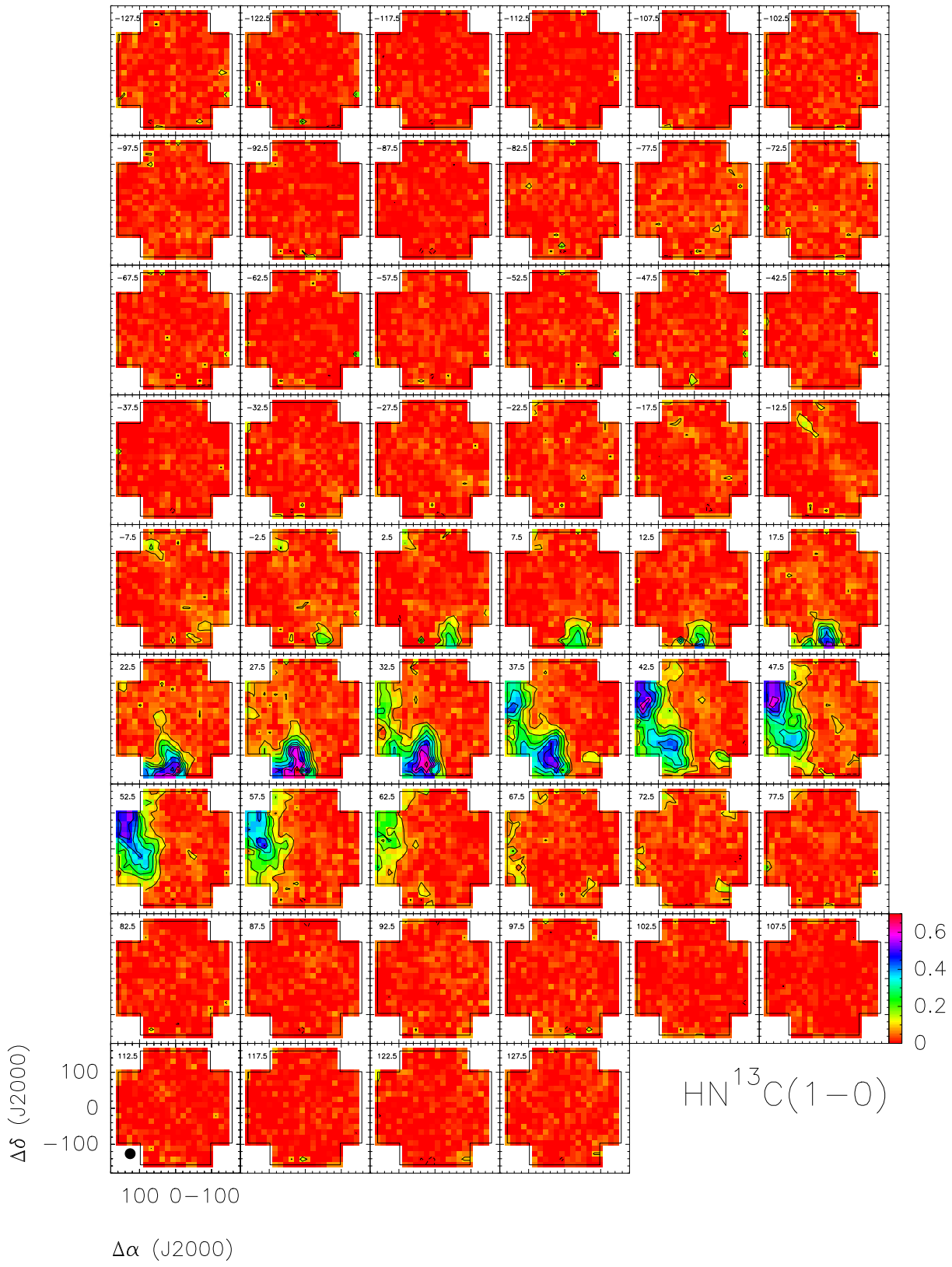

Fig. A.3. Same as Fig. A.2 but for the $HN^{13}C(1–0)$ emission.

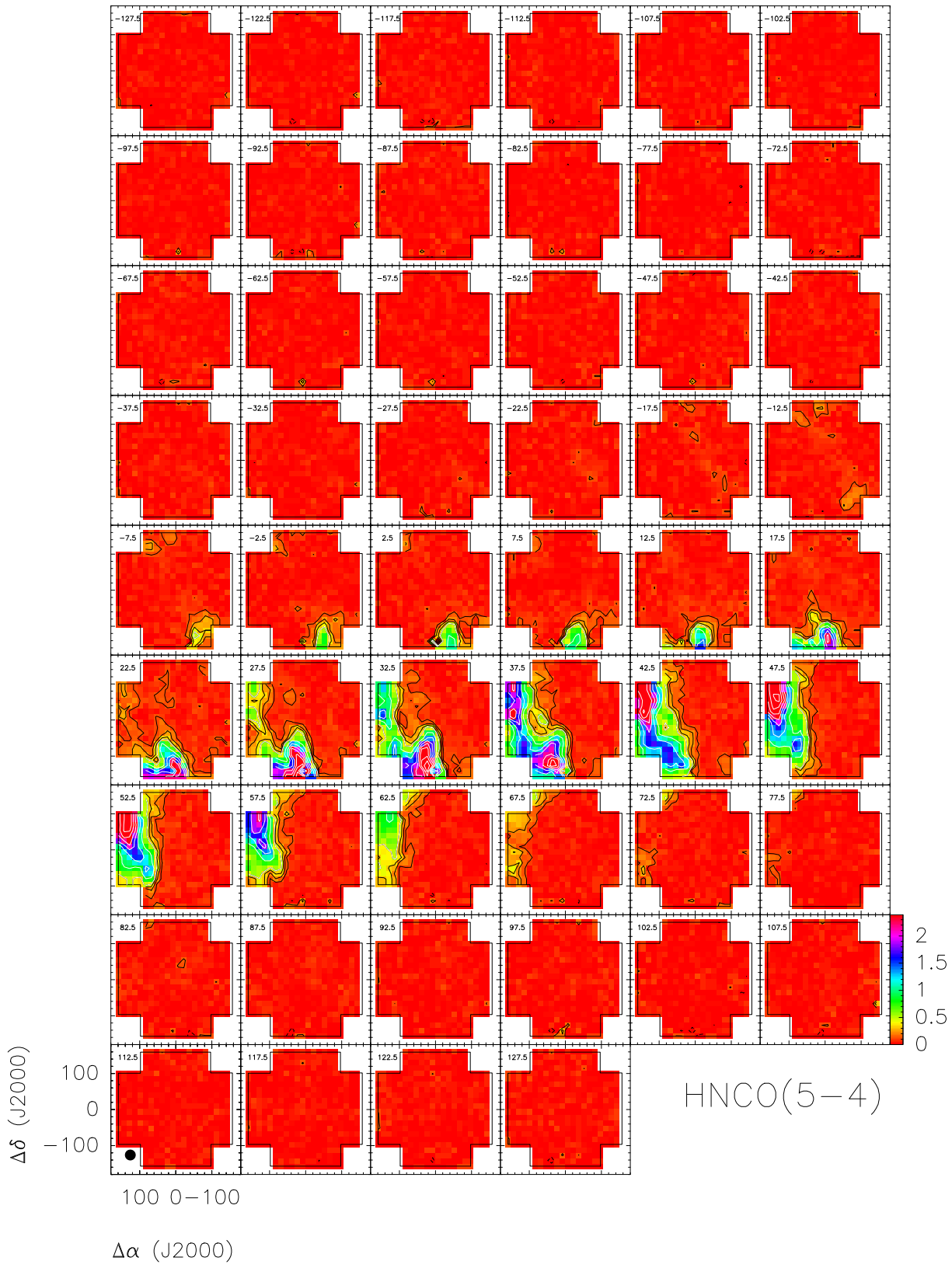

Fig. A.4. Velocity-channel maps of the HNCO($5_{0,5}$–$4_{0,4}$) emission. Black contour levels for the molecular line emission are from 0.11 K (3σ) to 0.44 K in steps of 0.11 K. White contour levels are from 0.44 K in steps of 0.44 K. In order to show more clearly the spatial distribution of the weak emission, the intensity scale has been saturated. The other characteristics of the figure are the same as in Fig. A.1.

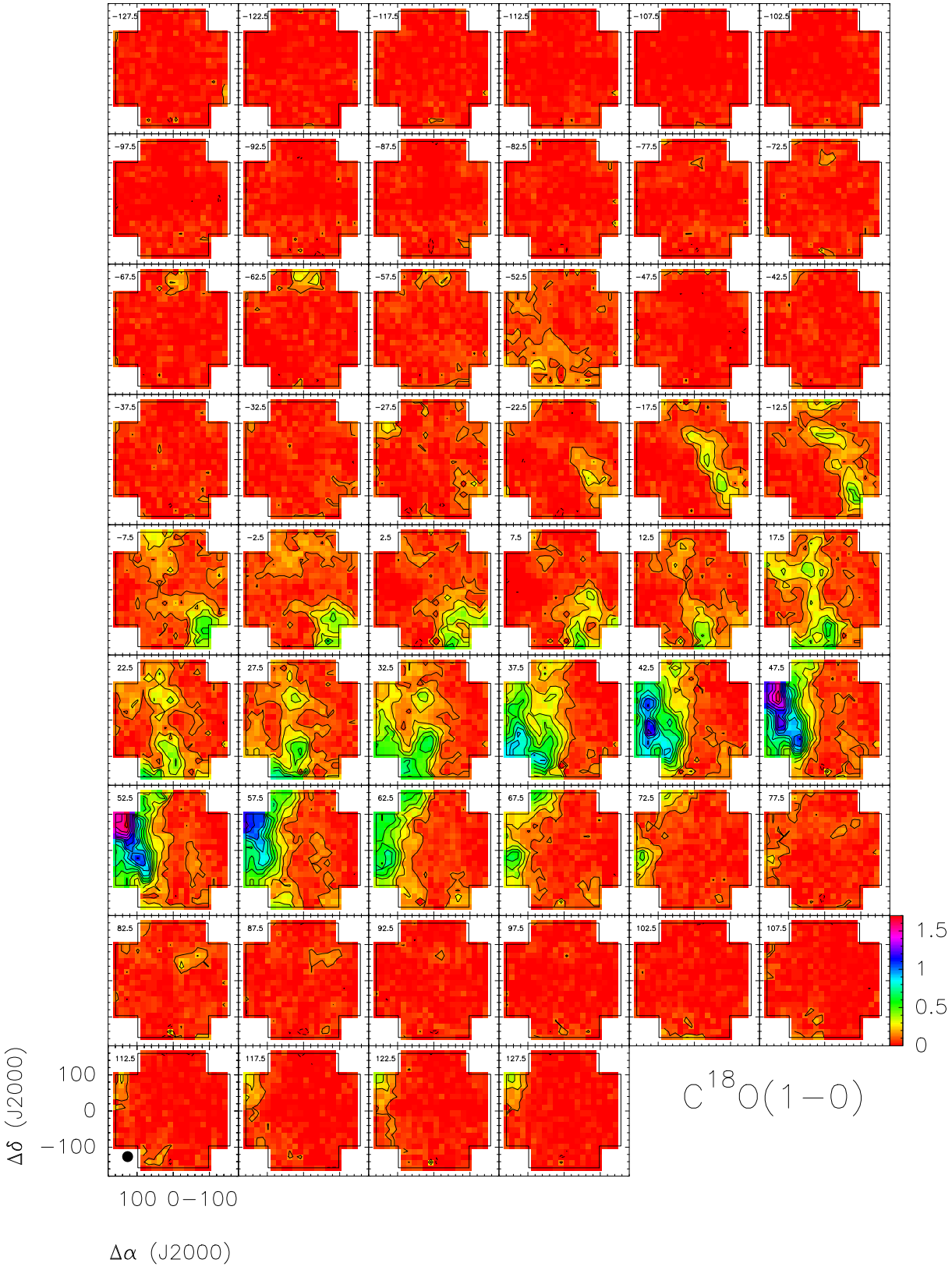

Fig. A.5. Velocity-channel maps of the $C^{18}O(1–0)$ emission. Contour levels for the molecular line emission are from 0.11 K (3σ) in steps of 0.11 K. The other characteristics of the figure are the same as in Fig. A.1.

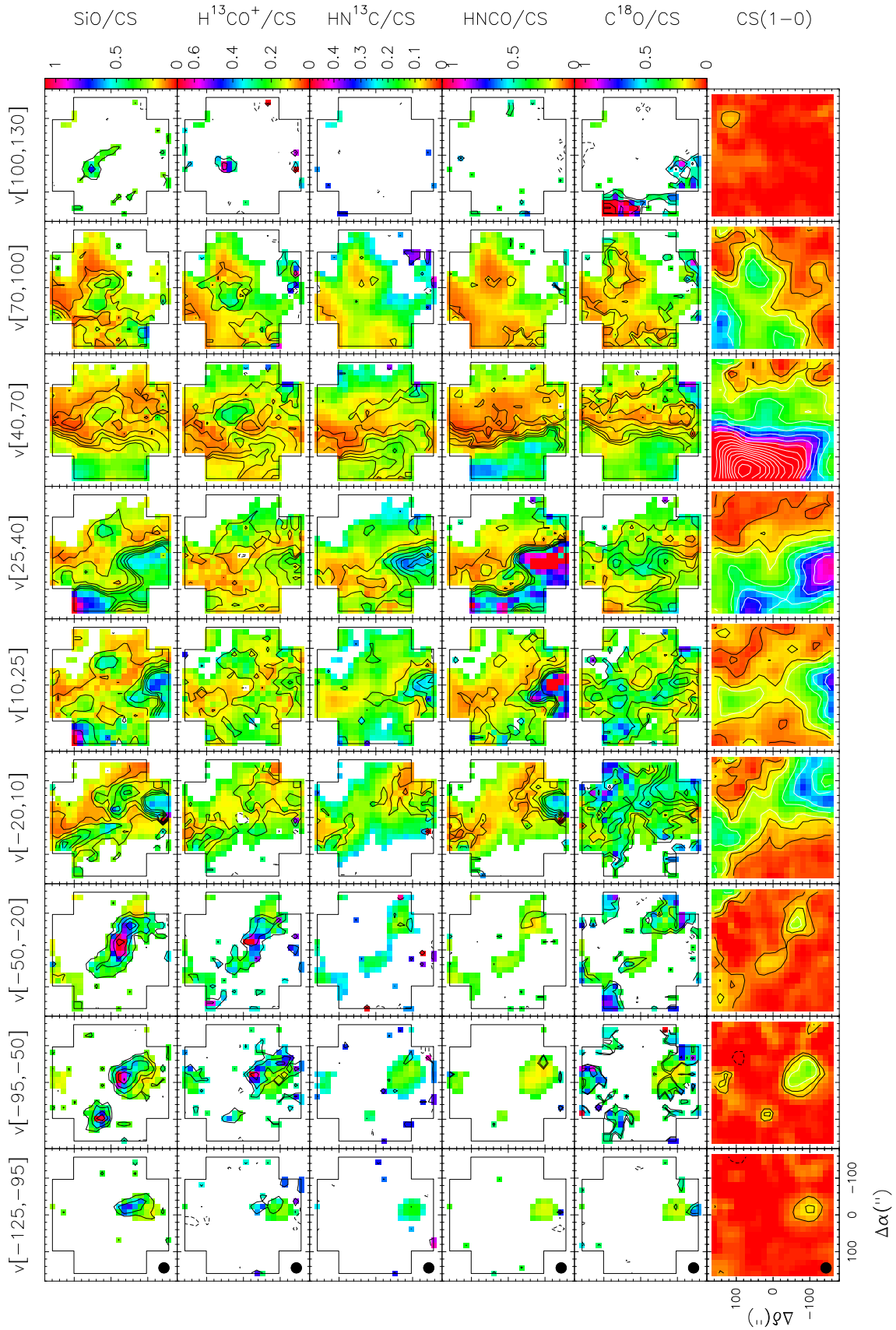

Fig. B.1. X/CS(1–0) intensity ratios in the same selected velocity ranges as Fig. 2. X stands for SiO(2–1), $H^{13}CO^+$(1–0), $HN^{13}C$(1–0), HNCO(5–4), and $C^{18}O$(1–0). Molecular emission is shown in contour levels, which are -3σ (dashed contour), 3σ, from 2.0 to 8 in steps of 1.5 K km s^{-1}. The 3σ level of each molecule is the same as in Fig. 2. Intensity ratio maps take upper and lower limits into account, using the 3σ value of each map as the limit value. The wedges to the left show the color scale of the different intensity ratios. Row at the bottom shows CS(1–0) maps of Tsuboi et al. (1999) to compare and show which pixels present meaningful ratios or are only limits (their contour levels and intensity scale are the same as in Fig. 2).